Formation and composition of organic aerosols from the uptake of glyoxal on natural mineral dust aerosols: a laboratory study

Francesco Battaglia[1,a], Paola Formenti[1], Chiara Giorio[2], Mathieu Cazaunau[3], Edouard Pangui[3], Antonin Bergé[3], Aline Gratien[1], Diana L. Pereira[1,b], Thomas Bertin[3], Joel F. de Brito[4], Manolis N. Romanias[4], Vincent Michoud[1], Clarissa Baldo[1,3], Servanne Chevaillier[3], Gael Noyalet[3], Philippe Decorse[5], Bénédicte Picquet-Varrault[3], and Jean-François Doussin[3]

[1] Université Paris Cité and Univ Paris Est Créteil, CNRS, LISA, F-75013 Paris, France
[2] Yusuf Hamied Department of Chemistry, University of Cambridge, Lensfield Road, Cambridge, CB2 1EW, UK
[3] Univ Paris Est Créteil and Université Paris Cité, CNRS, LISA, F-94010 Créteil, France
[4] IMT Nord Europe, Institut Mines-Télécom, Université de Lille, Centre for Energy and Environment, 59000, Lille, France
[5] Université Paris Cité, CNRS, Itodys, F-75013 Paris, France
[a] now at Dipartimento di Scienze Chimiche, Università degli Studi di Padova, Padova, Italy
[b] now at institute for Atmospheric and Earth System Research, University of Helsinki, Finland

For submission to Atmos. Chem. Phys.

Corresponding author: P. Formenti (paola.formenti@lisa.ipsl.fr)

Abstract

The uptake of glyoxal on realistic submicron mineral dust aerosol particles from a natural soil (Gobi Desert) is investigated during experiments in a large simulation chamber, under variable experimental conditions of relative humidity (RH), irradiation, and ozone concentrations. The uptake of glyoxal on the dust particles starts as soon as the glyoxal is injected in the chamber. At 80% RH, the measured uptake coefficient of glyoxal on mineral dust is $\gamma = (9 \pm 5) \times 10^{-3}$. The totality of the mass of reacting glyoxal is transformed in organic matter on the surface of the dust particles. The uptake of glyoxal is accompanied by the appearance of marker peaks in the organic mass spectra and a persistent growth in the volume concentration of the dust particles. While the mass of the organic matter on the dust rapidly reverts to values prior to uptake, the organic composition of the dust is modified irreversibly. Glycolic and other organic acids but also oligomers are detected on the dust. At 80% RH, compounds ranging from C_4 to C_{10} are observed as oligomerization products of glyoxal mono- and di-hydrate forms. The study suggests that dust aerosols could play a very substantial role in the formation of organic aerosols at high RH, but also that the reaction could have

potential important implications for the dust optical and hygroscopic properties, including their pH.

1. Introduction

Mineral dust originates naturally from the wind erosion of arid or semi-arid soils, resulting in the suspension of particles with diameters from fractions to hundreds of microns, which can be transported over thousands of kilometres whilst in the atmosphere (Adebiyi et al., 2023; Mahowald et al., 2014). The total global mass of mineral dust particles emitted annually in the atmosphere is of the order of 4600 Tg yr^{-1}, accounting for approximately 40% of the total annual aerosol emissions (Knippertz and Stuut, 2014; Kok et al., 2021). Major natural source areas of mineral dust are North Africa (~50% of the global annual dust emissions), Asia (~40%), North America, and the Southern Hemisphere (~10%; Kok et al., 2023). Anthropogenic emissions are associated with soil erosion for agriculture, pasture, and deforestation (Tegen and Fung, 1995; Webb and Pierre, 2018), but their contribution to the total annual dust mass loading is uncertain, ranging from 5 to 60% (Chen et al., 2023). Mineral dust significantly impacts the Earth's energy balance by absorbing and scattering radiation in the solar and terrestrial spectra (Di Biagio et al., 2019; Kok et al., 2023) and by influencing the lifetime and optical properties of mixed-phase and ice clouds (e.g., Atkinson et al., 2013; Harrison et al., 2001; Steinke et al., 2016). Current estimates of the effective radiative forcing (sum of direct and indirect) of natural mineral dust are in the range of -0.07 ± 0.18 W m^{-2} (Kok et al., 2023), owing to large uncertainties in the atmospheric mass loading and properties of dust at emission and during transport (Castellanos et al., 2024; Li et al., 2021).

Gas-particle interactions along the dust lifecycle contribute to these uncertainties. Numerous laboratory and field studies show that mineral dust is capable to adsorb various reactive gaseous compounds, which may modify its chemical composition, and in turn to alter optical properties, hygroscopicity and ice nucleation activity but also may affect the oxidative capacity of the atmosphere (Bauer et al., 2007; Chirizzi, 2017; Crowley et al., 2010; Joshi et al., 2017; Liu et al., 2013; Ooki and Uematsu, 2005; Romanias et al., 2012; Seisel et al., 2004; Tang et al., 2017; Turpin and Huntzicker, 1995; Usher et al., 2003; Wagner et al., 2008). Dust aerosol may promote photocatalytic reactions of inorganic gases such as SO_2 and NO_2, initiating nucleation events (Dupart et al., 2012; Nie et al., 2014).

The uptake of volatile organic compounds (VOCs) on mineral dust such as limonene, toluene (Romanías et al., 2016), isoprene (Zeineddine et al., 2017), phenol (Hettiarachchi and Grassian, 2024), and dicarboxylic acids (Ponczek et al., 2019), is also documented. These reactions may alter the VOC budget in the atmosphere and lead to the formation of secondary organic aerosols (SOA) (Li et al., 2019; Tang et al., 2017; Usher et al., 2003; Xu et al., 2023; Zeineddine et al., 2023), one of the key players of atmospheric chemistry (Shrivastava et al., 2017).

Glyoxal (CHOCHO) is one of the most abundant VOCs in the troposphere (Lewis et al., 2020). It is produced through the oxidation of aromatic compounds like benzene, toluene, and p-xylene (Volkamer et al., 2001) as well as by the photochemical oxidation of isoprene (Chan et al., 2017). The global atmospheric concentrations of glyoxal have been evaluated in the range of 10 – 100 pptv by Fu et al. (2008). However, case studies show sometimes higher concentrations. During a field study in Shanghai in the summer of 2018, Guo et al. (2021) reported an average glyoxal concentration of 164 ± 73 pptv, due to daytime photochemistry. Local concentrations of up to 400 pptv have been documented in regions influenced by aromatic pollution (Li et al., 2022). Satellite measurements of glyoxal show that the highest concentrations in tropical and sub-tropical regions are found during warm, dry periods influenced by biogenic emissions and vegetation fires, but also anthropogenic pollution (Vrekoussis et al., 2009). Elevated glyoxal concentrations have been observed in aged biomass burning plumes and tropical ocean regions, revealing model under-predictions in high-emission areas due to missing complex organic compound sources (Kluge et al., 2023). Field measurements in the northeast Atlantic Ocean reveal that models generally underestimate glyoxal concentrations due to missing contributions from acetaldehyde and other chemical precursors, and a potential glyoxal source from the ocean surface organic microlayer, particularly significant at night (Walker et al., 2022).

Glyoxal is a very soluble molecule which readily oligomerises in water, leading to the formation of larger molecules (Kalberer et al., 2004; Shapiro et al., 2009). Several previous studies have revealed that glyoxal has the ability to uptake onto aerosol particles, potentially serving as a significant source of organic aerosols (e.g., Liggio et al., 2005b, Carlton et al., 2007; Ervens and Volkamer, 2010; Galloway et al., 2009; Knote et al., 2014). The uptake of glyoxal on ammonium sulphate particles can lead to the formation of carbon-nitrogen compounds (such as imidazole derivatives),

oligomers, and organic acids (Galloway et al., 2009), that has been observed to cause browning (De Haan et al., 2020). The light-absorbing imidazole derivatives formed by glyoxal have been found to act as a photosensitizer, initiating radical chemistry under realistic irradiation conditions in the aerosol phase and initiating aerosol growth in the presence of limonene (Rossignol et al., 2014).

The study by Shen et al. (2016) revealed that glyoxal can also uptake onto synthetic minerals proxies of natural mineral dust, forming oligomers, organo-sulphates, formic acid, and glycolic acid, henceforth suggesting a potential significant mechanism for organic aerosol formation and modification of the optical and hygroscopic properties of mineral dust. Recently, Zogka et al. (2024) highlighted the dependence of the soil composition and size for the uptake of glyoxal on soils and soil surrogates (synthetic mineral).

Following up from those studies, in this paper we present novel laboratory experiments using a large-scale simulation chamber to investigate the formation of organic aerosol from the uptake of glyoxal on realistic airborne mineral dust particles, in atmospherically-relevant conditions. Dust aerosols are generated from a natural parent soil from the Gobi Desert, one of the most important sources of tropospheric dust and representative of an area where this interaction could take place (Wang et al., 2015).

This paper has two major objectives. First, it provides experimental observations of the uptake of glyoxal on mineral dust aerosol, leading to the formation of organic aerosol mass upon interaction and measuring glyoxal uptake coefficient of mineral dust. Secondly, it presents the chemical composition of the mixed organic-dust aerosols, in terms of its oxidation state, molecular composition and the evolution of SOAcontent from glyoxal.

2. Experiments and methods

This study uses the CESAM atmospheric simulation chamber (CESAM – Chambre de Simulation Atmosphérique Multiphasique, which translates to Experimental Multiphasic Atmospheric Simulation Chamber in English), a 4.2 m^3 cylindrical stainless-steel reactor initially described by Wang et al. (2011). CESAM was specifically designed to study multiphase processes involving aerosol particles, gas-phase compounds and water, both in the vapour and liquid phases (Brégonzio-Rozier et al., 2016; Denjean et al., 2014; Giorio et al., 2017). CESAM is equipped with three

6.5 kW high-pressure arc xenon lamps (model EX-170GM3-E, IREM SpA, Borgone, Italy) and 6 mm Pyrex plate filters to mimic the solar radiation. A 50 cm stainless-steel four-blade fan located at the bottom of the chamber ensures a mixing time of about 1 minute for the gas phase and the homogeneity of the internal composition.

2.1. Injection and cleaning protocols

Dust aerosols were generated and injected into the chamber according to the protocol detailed in Battaglia et al. (2025) using a natural soil sample from the Gobi Desert (107.48°N; 36.49°E). Prior use, the soil was sieved at 1000 µm and dried at 100°C for less than one hour to remove adsorbed water and contamination from volatile gases. A quantity ranging from 30 and 50 g was placed in a 1 L Büchner flask and shaken at 100 Hz using a sieve shaker (Retsch® AS200) to simulate the saltation and sandblasting mechanisms through which wind erosion generates airborne dust in the real atmosphere (Di Biagio et al., 2017). An Aerodynamic Aerosol Classifier (AAC, Cambustion®) was placed between the dust generator and the chamber to inject mono-modal dust centred between 300 and 400 nm in geometric diameter.

Glyoxal was prepared by heating a mixture of equal amounts of its trimer hydrate (Fluka® Analytical) and P_2O_5 (Sigma – Aldrich ReagentPlus®, 99%) at 150°C (Horowitz et al., 2001). The trimer decomposition occurs inside a vial connected to a vacuum gas manifold. Glyoxal was collected as yellow crystals in a second vial immersed in an ethanol – liquid nitrogen cold trap at around -90°C and then vaporised in a 2.1 L glass bulb to a controlled pressure. This vial was connected to the simulation chamber to inject the glyoxal through a pure nitrogen flow.

Ozone was generated by a Corona discharge in pure O_2 using a commercial dielectric ozone generator (MBT 802N, Messtechnik GmbH, Stahnsdorf, Germany). Water vapour was generated by heating ultrapure water (Milli-Q IQ 7000, Merk™) inside a pressurised stainless-steel vessel, previously rinsed at least three times. The total organic carbon (TOC) content of the ultrapure water was monitored to evaluate the influence on the production of organic particles, which was found to be minor (see **Text S1** in the Supplementary Material). The relative humidity (RH) inside the chamber was measured by a HMP234 Vaisala® humidity and temperature transmitter. Before each experiment, the chamber was evacuated down to 10^{-4} mbar and then filled with a mixture of 80% N_2 (Messer, purity > 99.995%) and 20% O_2 (Linde 5.0, purity 99.999%)

172 to an internal pressure exceeding by about 5 to 10 mbar the room atmospheric
173 pressure, to prevent accidental contamination during the experiments.

2.2. Instrumentation

175 The CESAM chamber was equipped with a suite of standard instrumentation for the
176 detection of the aerosol and the gas-phase, whose details are reported in **Table S1**.

177 Gas-phase glyoxal was measured by a combination of in-situ long-path Fourier
178 Transform Infra-Red (FTIR) spectrometry (Bruker Tensor 37) in the 2720-2930 cm^{-1}
179 absorption band corresponding to the C–H bonds, by a Cavity Attenuated Phase Shift
180 (CAPS) NO_2 analyser (Model T500U, from Teledyne API) and a Proton Transfer
181 Reaction-Time Of Flight-Mass Spectrometer (PTR-ToF-MS) (KORE Technology®,
182 second generation) operated in H_3O^+ ionization mode for VOC detection. The FTIR
183 spectrometer provided also with the concentrations of formic acid (HCOOH), measured
184 in the C-O bond vibration band centred at 1105 cm^{-1}; ozone (O_3) measured in the
185 asymmetric stretching of the absorption band centred at about 1043 cm^{-1}; and carbon
186 monoxide (CO), detected at about 2143 cm^{-1}. The standard infrared absorption spectra
187 of the compounds used for quantification, along with the specific absorption bands
188 integrated for their quantification, are shown in **Figure S1**. CO and carbon dioxide
189 (CO_2) were additionally measured by an APEE ProCeas® analyser. Nitrogen oxides
190 (NO_x) were monitored by APNA-370 analyser by Horiba®.

191 The aerosol total number concentration above 2.5 nm was measured by a
192 Condensation Particle Counter (TSI® model 3075). The aerosol number size
193 distribution in the submicron fraction was measured by a combination of a Scanning
194 Mobility Particle Sizer (SMPS) consisting of a Differential Mobility Analyser (TSI®,
195 model 3080) coupled with a Condensation Particle Counter (TSI® model 3072) and an
196 Optical Particle Counter (sky-GRIMM® OPC model 1.109).

197 The aerosol chemical composition was measured by a combination of online and
198 offline methods. A Time-of-flight Aerosol Chemical Speciation Monitor (ToF–ACSM,
199 Aerodyne Research Inc.) equipped with a standard vaporiser provided quantitative
200 unitary mass resolution spectra between 40 nm and 1 μm vacuum aerodynamic
201 diameter (Fröhlich et al., 2013). The instrument was operated through a Nafion
202 membrane dryer (model PD-50T-12). The organic mass concentration (m_{org}) was

203 obtained considering a unitary collection efficiency (CE = 1) and a relative ionization
204 efficiency (REI) of 1.4 (Nault et al., 2023).

205 The glyoxal fragment CH_2O^+ at m/z 30 has an isobaric interference with the NO^+
206 fragment from nitrate. Following Galloway et al. (2009), the contribution of nitrate to
207 the total signal at m/z 30 was calculated as 1.7 times the intensity of the nitrate signal
208 at m/z 46, which corresponds to the 30/46 signal ratio measured during nitrate
209 calibration. The contribution to m/z 30 of glyoxal was then calculated from the total
210 signal by subtracting the contribution of the nitrate and the contribution of air. The
211 elemental ratios of the organic fraction O/C and H/C are calculated from the measured
212 f_{44} and f_{43} respectively, following the parametrizations proposed by Aiken et al. (2008)
213 and Ng et al. (2011), respectively.

214 Filter samples were collected on PTFE filters (Zefluor, 47 mm diameter, 2 µm pore
215 size, Pall Life Sciences) and quartz fiber membranes (Tissuquartz 2500 QATUP, 47
216 mm diameter, Pall Life Sciences) using a series of custom-made stainless-steel holder
217 of 6-mm diameter operated at 10 L min^{-1}, and preceded by an denuder filled with active
218 charcoal paper to remove ozone and VOCs. The sampling time ranged from 30
219 minutes to 3 hours. The filter holders and PTFE filters were pre-cleaned with
220 dichloromethane (99.8 %, HPLC grade) in an ultrasonic bath, while the quartz filters
221 were pyrolyzed at 550°C for approximately 8 hours. After sampling, filters were folded
222 and placed in an aluminium paper envelope previously pyrolyzed (same protocol than
223 the filters), and stored in a refrigerator at -18°C. Chamber blanks were collected by
224 sampling for about 20 min from the chamber only filled with N_2 and O_2. Analytical
225 blanks were also collected.

226 **2.3. Filter analysis**
227 The analysis of the filter samples was conducted by a combination of three techniques
228 to provide with a comprehensive view of the chemical composition of the organic
229 fraction formed on the dust particles as the result of the processing by glyoxal. The full
230 details of the analysers and analytical protocols are reported in as detailed in **Text S2**
231 in the supplementary material. Those include

232 1/ the Supercritical fluid extraction coupled with gas chromatography mass
233 spectrometry (SFE/GC-MS; Chiappini et al. (2006)) for target analysis of low-

weight mass fragments derived from molecules linked to glyoxal reactivity (see **Table S2.1** in the Supplementary Material);

2/ Electrospray ionization (ESI) high-resolution mass spectrometry (Kourtchev et al., 2015) was used to obtain high-resolution mass spectra and formulae assignments for low-volatility compounds in the ranges m/z 50–500 and m/z 150–1000 (Zielinski et al., 2018). These were processed to provide with parameters describing the carbon oxidation, through O/C and H/C bulk ratios, and the identification of molecular groups such as CHO, CHON, CHOS, CHNS, and CHONS. ESI-HR-MS was also used for a screening analysis of molecules resulting from the glyoxal transformation due to hydration, oxidation, and oligomerization. These included formulas for mono- and dihydration products ($C_2H_4O_3$ and $C_2H_6O_4$, respectively), oxidation products (formic acid (CH_2O_2), glycolic acid ($C_2H_4O_3$), glyoxylic acid ($C_2H_2O_3$), and oxalic acid ($C_2H_2O_2$)), and oligomers formed by the hydrolysis of hydrated glyoxal formulas (linear oligomers with generic stoichiometric formula $C_{2n+2m}H_{4n+6m-2(n+m-1)}O_{3n+4m-(n+m-1)}$, and ring oligomers with generic formulae $C_{2n+2m}H_{4n+6m-2(n+m)}O_{3n+4m-(n+m)}$).

3/ X-ray photoelectron spectrometry (XPS) was used following Denjean et al. (2015) to quantify the elemental O/C ratio of the particle surface (O/C_{surf}) to a depth less than 10 nm. The O/C_{surf} was calculated as, as explained in Text S2 in the Supplementary Material. The XPS measurement on a filter collected during one ageing experiment are shown as an example in **Figure S2.1** in the Supplementary Material.

2.4. Calculation of the aerosol size distribution

The procedure for combining the measurements of the SMPS and the sky-GRIMM® OPC is based on Baldo et al. (2023) and it is described in detail in Battaglia et al. (2025). The number size distributions, expressed in dN/dlog$D$ (cm^{-3}), are used to evaluate the total particle surface S (µm^2 cm^{-3}) and volume V (µm^3 cm^{-3}) by assuming spherical particles as

$$S = \int \pi D^2 \frac{\mathrm{d}N}{\mathrm{dlog}D} \ \mathrm{dlog}D \tag{2}$$

$$V = \int \frac{\pi}{6} D^3 \frac{\mathrm{d}N}{\mathrm{dlog}D} \ \mathrm{dlog}D \tag{3}$$

265

2.5. Calculation of the glyoxal uptake coefficient and rate of particle formation

The uptake coefficient (γ) is defined as the probability of the gas to be taken up on the aerosol surface. It is a unit-less parameter expressed by the ratio between the number of molecules taken up on a surface and the total number of collisions of the gas on the surface as

$$\gamma = \frac{number\ of\ total\ molecules\ taken\ up}{total\ number\ of\ collisions} \tag{4}$$

The gas-phase uptake coefficient (γ) was estimated from the first-order heterogeneous loss rate of glyoxal (k_{het}, s^{-1}) as

$$\gamma = \frac{k_{het}}{\omega} \tag{5}$$

The rate of collisions (collision frequency, ω) is the defined as

$$\omega = \frac{cA_s}{4} \tag{6}$$

where:

- $c = 146 \times \sqrt{\frac{T}{MW}}$ is the mean molecular speed (m s^{-1}), where T is the air temperature (here 298 K) and MW the molecular weight of the compound of interest (in the case of glyoxal MW = 58 g mol^{-1}).

- A_s is total aerosol surface concentration (m^2 m^{-3}).

The total aerosol surface concentration (A_s) is calculated from the aerosol size distribution recorded at the end of the dust injection.

The heterogeneous loss rate of glyoxal (k_{het}) due to its uptake on dust particles can be determined as the difference of the loss rate of glyoxal measured during the uptake experiments (k_{obs}) and the glyoxal loss rate on the chamber walls (k_{loss}) as

292

$$k_{het} = k_{obs} - k_{loss} \qquad (7)$$

The glyoxal wall loss is represented by a partition equilibrium described by two first-order reactions: one for the adsorption of gas phase molecules onto the chamber walls, and one for the reverse process. The rate constants for both processes have been obtained experimentally through control experiments with only glyoxal in the chamber and at different relative humidity conditions, as detailed in **Text S3** in the supplementary material.

If the uptake reaction is of the first rate, k_{het} is henceforth calculated as

$$k_{het} = \frac{ln\left(\frac{[Gly]_0}{[Gly]_{obs}}\right) - ln\left(\frac{[Gly]_0}{[Gly]_{loss}}\right)}{t} \qquad (8)$$

where $[Gly]_0$ is the initial concentration of glyoxal, $[Gly]_{obs}$ represents the observed evolution of glyoxal concentration in time, resulting from the sum of uptake and wall loss, and $[Gly]_{loss}$ represents the estimated glyoxal concentration resulting from the wall loss.

The rate of formation of the particulate organic matter (POM; k_{F-POM}) due to the uptake of glyoxal on the dust can be calculated as

$$k_{F-POM} = \frac{ln\left(\frac{[POM]_t}{[POM]_0}\right)}{t} \qquad (9)$$

where $[POM]_0$ represents the initial POM concentration in the particle phase, and $[POM]_t$ represents the concentration of the POM formed at a given time.

In the hypothesis that the POM formation is solely due to the uptake of glyoxal, γ can be also evaluated as

$$\gamma = \frac{k_{F-POM}}{\omega} \qquad (10)$$

319

3. Results and discussion

3.1. Overview of experiments

The ageing experiments of monodispersed mineral dust and glyoxal described in this paper are summarised in **Table 1**. All the aerosol data are corrected for dilution, wall loss, and particle loss through the tubing systems as detailed in **Text S4** in the Supplementary Material. Gas phase concentrations are corrected for dilution only.

326

Table 1. Listing and initial conditions of the experiments considered in this study, including experiments with glyoxal only (experiment type GL), ammonium sulphate and glyoxal (AS + GL), dust only (D) and dust with glyoxal (D + GL). The glyoxal and ozone gas phase concentrations correspond to the maximum value measured by FTIR after the respective injections. V_{seed} indicates the maximum volume concentrations of seed particles (either dust or ammonium sulphate) measured after the particle injection. The notation "dark/light" indicates experiments when filter samples were collected both in the dark and with irradiation.

Experiment type	Reagents	Date	Experiment number	RH, %	Light	$[O_3]$, ppb$_v$	Temp, K	$[GL]$, ppb$_v$	V_{seed}, µm^3 cm^{-3}
Control	GL	29/04/2021	G_1	< 5	dark	---	292	1130	---
		11/02/2022	G_2	77	light	1440	291	627	---
	AS+GL	21/02/2023	AS_1	38	dark	---	298	527	50.1
		23/02/2023a	AS_2	35	dark	---	298	516	48.3
		23/02/2023b	AS_3	32	light	---	298	445	64.8
		07/09/2023	AS_4	81	light	---	301	779	304.1
		08/09/2023	AS_5	83	light	---	300	430	161.2
	D	31/01/2022	D_1	< 5	dark/light	---	292	---	31.5
		03/02/2022	D_2	75%	dark/light	---	293	---	55.4
Uptake	D+GL	04/02/2022	D_3	< 5	dark/light	---	293	690	35.6
		08/02/2023	D_4	32	dark	---	294	940	21.5
		09/02/2023	D_5	31	light	---	295	1050	52.7
		10/02/2023	D_6	35	dark	---	294	809	37.4
		13/02/2023	D_7	34	light	---	296	850	51.3
		30/04/2021	D_8	76	light	---	289	759	28.3
		03/05/2021	D_9	79	light	---	290	607	38.7
		04/05/2021	D_{10}	81	light	---	290	371	31.5
		05/05/2021	D_{11}	78	dark	---	291	805	30.1
		06/05/2021	D_{12}	82	dark	---	292	432	21.1
		08/02/2022	D_{13}	81	dark/light	1270	293	555	64.0
		09/02/2022	D_{14}	78	dark/light	1450	293	756	79.8
		10/02/2022	D_{15}	75	dark/light	---	295	600	68.4
		14/02/2023	D_{16}	83	dark	---	296	661	35.8
		15/02/2023	D_{17}	75	light	---	298	444	41.0

334

335 **Table 1** also lists the few control experiments using ammonium sulphate as seed

336 particles, described in detail in **Text S5** in the Supplementary Material. No POM

337 formation was observed during control experiments with dust or glyoxal only, both dry

338 and humid conditions and with and without irradiation.

3.1.1. Timeline of particle concentration and composition

340 The ageing experiments lasted up to five hours. For the experiments carried out in wet

341 conditions, the injection of water vapour preceded the injection of dust. The injection

342 of glyoxal (nominal concentration of 1 ppmv) was conducted at least after 30 minutes

343 after the dust to ensure that the dust particles were homogenously distributed in the

344 reactor. Irradiation was started within one hour after the glyoxal uptake onto the

345 particles. On a few experiments, ozone was injected before glyoxal to verify the

346 sensitivity of the reactions to the presence of an oxidant.

347 The typical timelines of the particle concentrations (number and volume) and the non-

348 refractory composition measured in dry conditions and at 30% and 80% relative

349 humidity are shown in **Figure 1**.

350
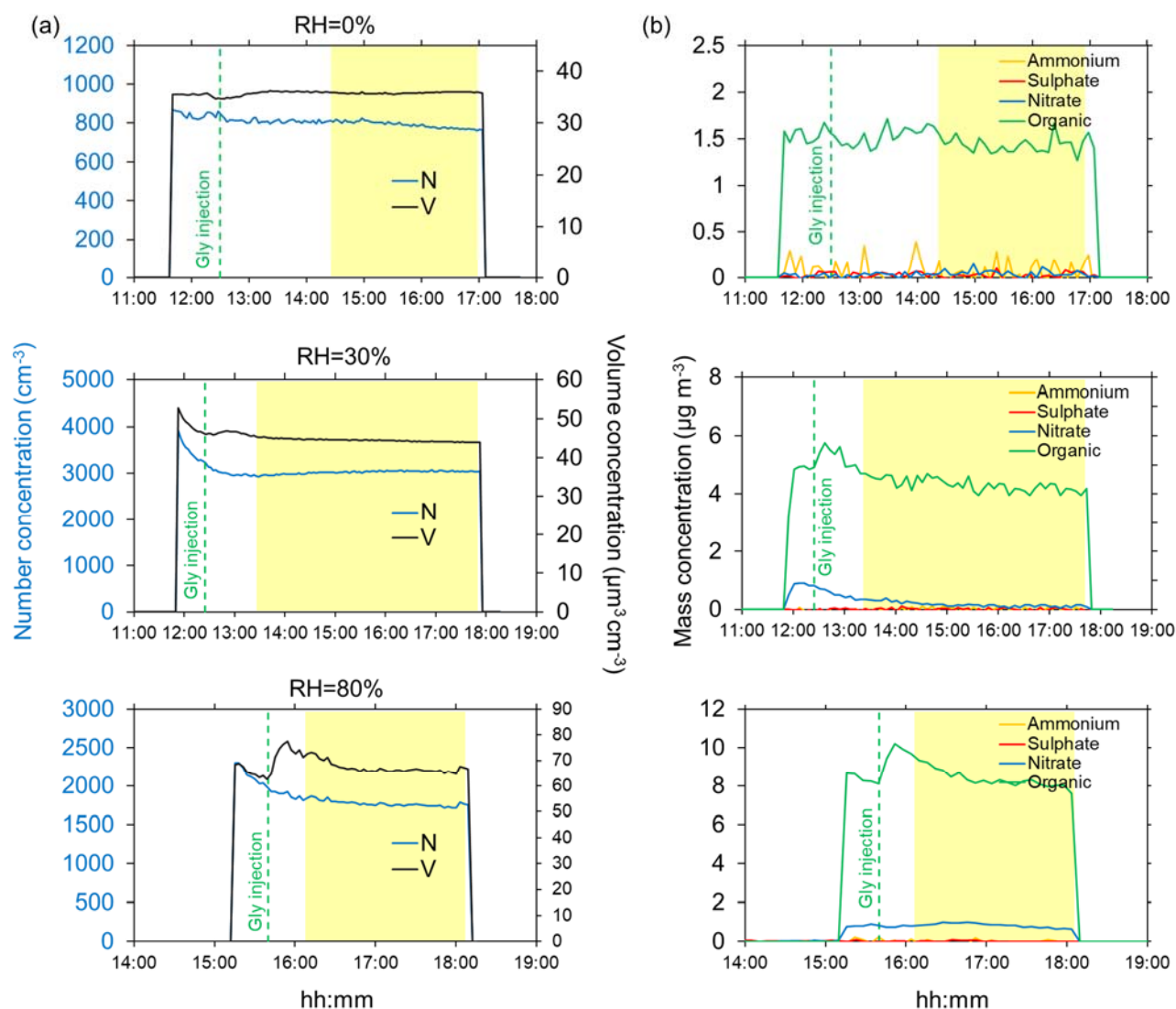
Figure 1. Timeline of ageing experiments of submicron dust with gas-phase glyoxal in dry conditions (top, experiment D_3), 30% (middle, experiment D_7), and 80% RH (bottom, experiment D_{15}). Left (a): aerosol total number (N) and volume (V) concentrations (blue and black lines, respectively) calculated from the measured dust size distributions. Right (b): mass concentrations of ammonium, sulphate, nitrate and organic (yellow, red, blue and green lines, respectively) measured by the ACSM. The yellow-highlighted portion of the graph indicates the interval where irradiation takes place, while the green vertical dashed lines indicate the injection glyoxal in the chamber. The dust injection corresponds to the time of the initial increase of the number and volume concentrations. Aerosol time series are corrected for dilution, wall loss and particle loss through the tubings.

Figure 1 shows that in dry conditions, there is no significant variation of either the aerosol number or the volume concentrations, nor the chemical composition (including organics) following the glyoxal injection.

At 30% RH, a small increase in the total volume concentration (approximately 5 μm^3 cm^{-3}) is observed for about 30 minutes after the injection of glyoxal. This corresponds to an increase of the POM of about 1 $\mu g\ m^{-3}$, approximately 20% more with respect to

the value measured before the uptake. On the other hand, the particle number concentration shows an apparent decrease at the beginning of the experiments, possibly because the particle loss correction model of Lai and Nazaroff (2000) does not fully apply to dust particles and humid conditions (see discussion in Battaglia et al. (2025). After that, and through the duration of the experiment, however, it remains constant, indicating that the increase in the particle volume occurs on the dust particles and not because of new particle formation.

At 80% RH, the increase in both the total volume and the POM concentrations is more pronounced, approximately 10-15 μm^3 cm^{-3} and 2 μg m^{-3}, respectively. As for 30% RH, both total particle volume and the POM concentrations return to values observed prior the injection of glyoxal, within approximately 30 minutes from their maximum values, likely due to evaporation. A similar behaviour is observed in the presence of ozone (**Figure S2** in the Supplementary Material). As for 30% RH, the particle number concentration slightly decreases in time at the beginning of the experiment, but then remains constant, again excluding the formation of new particles but rather confirming the formation of organic matter on pre-existing particles. This is also supported by the fact that the rate of increase of POM and particle volume is the same (slope 3.2×10^{-4} s^{-1} and 3.2×10^{-4} s^{-1}, respectively for POM and total volume), as shown by **Figure S3** in the Supplementary Material.

3.1.2. Timeline of gas-phase concentration

Figure 1 shows also that, while sulphate and ammonium are never detected, a background concentration of nitrate up to 1 μg m^{-3} is measured by the ACSM as soon as the dust particles are injected in the presence of water. We attribute it to the heterogeneous interaction between NO_2 and the dust particles (Goodman et al., 1999) as indeed, a background concentration of a few ppb of NO_2 is present in the chamber as a result of the procedure used to reduce the TOC content in the injected water (see **Figure S4** in the Supplementary Material). However, since the contribution of nitrate represents at maximum 1% of the injected dust mass and whether decreases or remains constant throughout the experiment, its contribution to the particle growth and overall ageing of the mineral dust should be negligible.

Figure 2 shows the time series of the gas-phase compounds detected during the same experiment (D_{15}) at 80% RH.

400
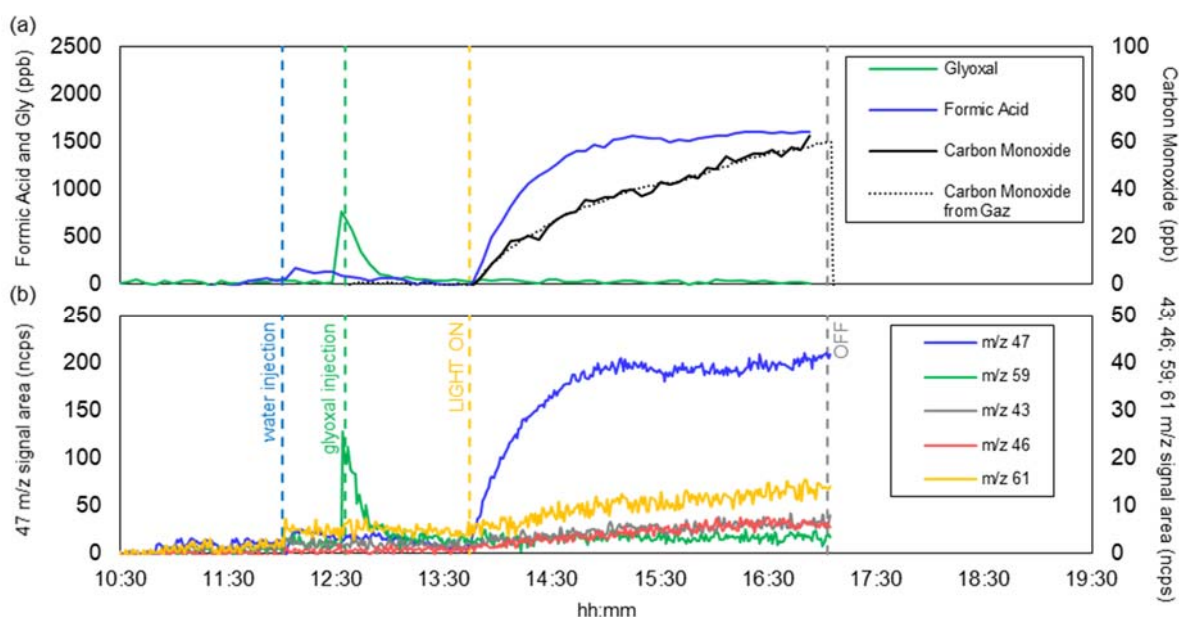
Figure 2. Time series of the gas-phase composition observed during experiment D_{15}: (a) concentrations of carbon monoxide, glyoxal and formic acid measured by FTIR (for CO the measured of the online analyser are also shown); (b) various VOC ions (m/z 47, 59, 43, 46 and 61) measured by the PTR-MS. Ion signals measured by PTR-MS are normalized by signals of reagent ions (i.e. H_3O^+ and $H_3O^+(H_2O)$) and therefore expressed in normalized counts (ncps). The blue vertical dashed lines indicate the injection of water in the chamber; the green vertical dashed lines indicate the injection of glyoxal in the chamber, the yellow dashed lines indicate the beginning of irradiation and the grey dashed lines indicate the end of irradiation.

The measured glyoxal concentration after the injection (**Figure 2a**) is lower than the nominal concentration of 1 ppm and goes to zero within minutes due to the rapid interactions with the walls of the chamber, water vapour, and the dust particles. Upon irradiation, formic acid and carbon monoxide are formed, as expected by the photolysis of glyoxal (De Haan et al., 2020). Fragments m/z = 46 and 47 are observed during water injection and photolysis, which could originate from the deprotonated and protonated form of formic acid, respectively. This suggests that a minor fraction of the formic acid could result from the desorption of compounds (including glyoxal) from the chamber walls. Fragments m/z = 43 and m/z = 61, and occasionally m/z = 45 (not seen during experiment D_{15} and therefore not shown in **Figure 2b**), are observed at a normalised intensity two orders of magnitude lower than that of formic acid, but not attributed. The quantification with both PTR-MS and FTIR in our experimental RH conditions is complex due to water presence, which reduces the sensitivity of PTR-MS and can interfere with the absorption of various organic compounds, making their quantification less accurate.

3.2. Evaluation of glyoxal uptake coefficient and rate of formation of organic aerosols

Figure 3 shows an example of the temporal evolution of the natural logarithm of the glyoxal concentration measured by the FTIR, compared to that measured during a typical blank experiment without dust particles (top panel) and the variation of the aerosol organic fraction measured by the ToF-ACSM during the same time period (lower panel).
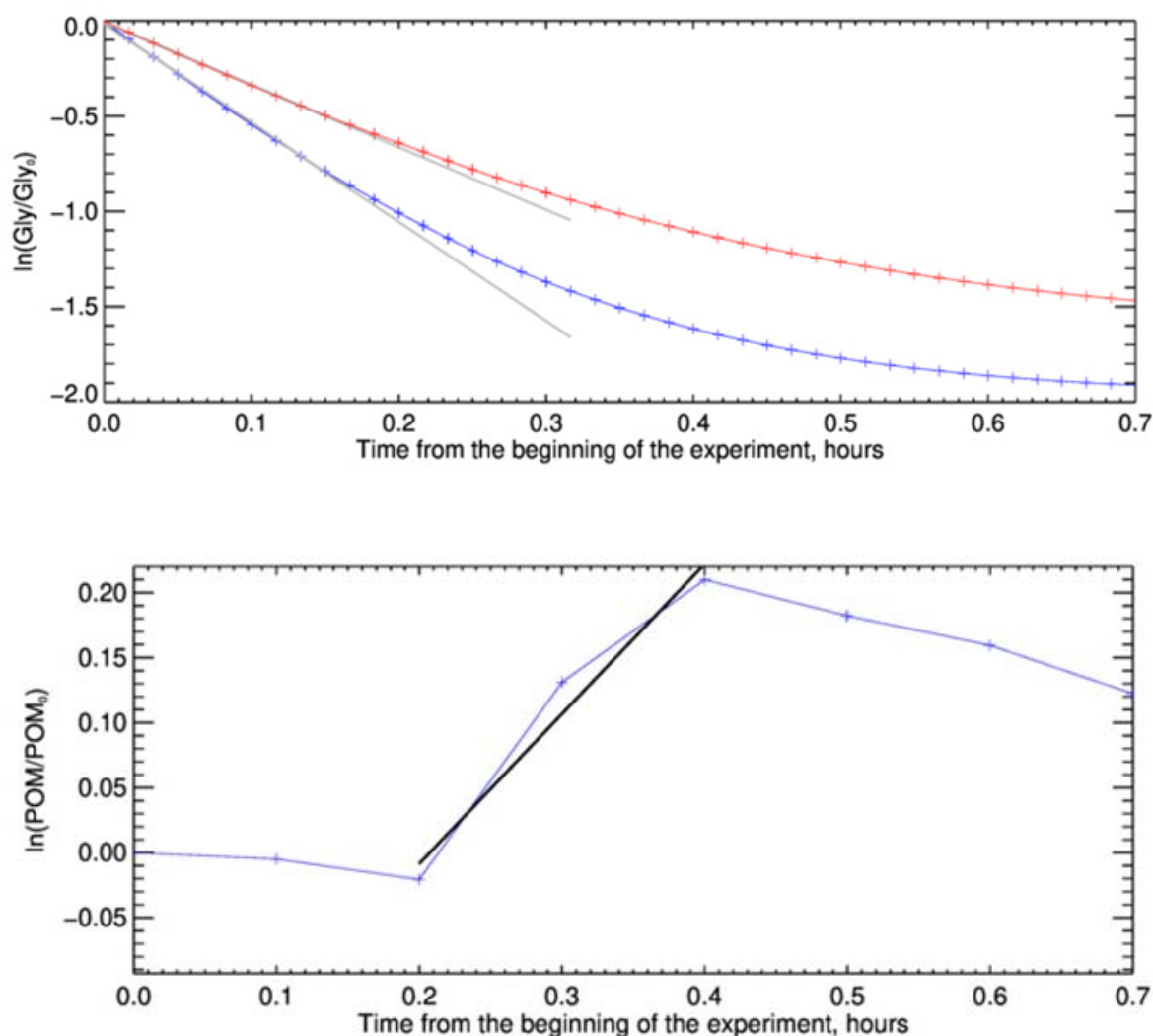
Figure 3. Measurement of glyoxal uptake coefficient on dust for the experiment D_{15}, conducted at 80% RH. The figure compares the two methods for measuring the uptake coefficient. In the top image, results are shown for the method based on monitoring the decay of gas-phase glyoxal. The red and blue curves represent the logarithm of the ratio between the calculated decay of gas-phase glyoxal in the absence and presence of dust aerosols, respectively. The black lines represent the linear fit whose slope provides the heterogeneous kinetic constants of the two processes. The image at the bottom displays the result of the uptake coefficient measurement for the same experiment, obtained from the organic formation on the dust aerosol monitored by the ToF-ACSM. The blue time series shows the logarithm of the ratio between the measured organic concentration divided by the initial organic on dust aerosol, while the black line is the linear fit representing the kinetics of organic formation.

Within the first 10 minutes after the injection of glyoxal, the decrease of the natural logarithm concentrations ratio with time in the presence of dust is linear (that is, the rate is constant). After that, the loss slightly deviates from linearity. The difference from linearity is more evident for the blank experiment, when it occurs earlier than when the dust is present. These observations indicate that, within the first 10 minutes, the uptake of glyoxal on the dust particles can be considered to follow a first-order kinetic and its rate represents an initial uptake coefficient. In the following 20 minutes approximately, the uptake slows down, possibly because all the sites available on the particle surface become occupied, but also because that desorption from the particle surface could reinject glyoxal in the reactive mixture. On the particle phase, the natural logarithm of the organic concentration, normalised by its initial value increases rapidly and linearly, almost on the same time scale of that of the loss of glyoxal, but then decreases to return to its initial value within approximately one hour. These observations confirm that the uptake of glyoxal results in a formation of OA on the dust particles, but that this process is reversible.

The uptake coefficients calculated as the linear fit of the glyoxal and particle organic concentration are presented in **Table 2**.

Table 2. Uptake coefficients for glyoxal on mineral dust and ammonium sulphate calculated from the loss of gas-phase glyoxal and the rate of OA formation for the experiments conducted at 80% RH. The initial glyoxal concentration is reported. The aerosol surface concentration (A_s) corresponds to the value preceding the glyoxal injection. Ozone concentration is the maximum concentration measured by FTIR spectroscopy after the injection. For ammonium sulphate, only the γ values calculated from the loss of gas phase glyoxal are presented, as the ACSM collection efficiency (CE) for ammonium sulphate varies significantly during OA formation (Matthew et al., 2008).

Date	Experiment ID	RH%	$[GL]_0$, ppb$_v$	Ozone (ppb)	A_s ($m^2\ m^{-3}$)	ω (s^{-1})	γ_{gas}	$\gamma_{OA\ glyxoal}$
30/04/2021	D_8	76	759	---	4.8×10^{-4}	3.9×10^{-2}	6.0×10^{-3}	1.0×10^{-3}
03/05/2021	D_9	79	607	---	6.1×10^{-4}	5.0×10^{-2}	1.5×10^{-2}	1.5×10^{-2}
04/05/2021	D_{10}	81	371	---	5.1×10^{-4}	4.2×10^{-2}	1.7×10^{-2}	9.0×10^{-3}
05/05/2021	D_{11}	78	805	---	4.6×10^{-4}	3.8×10^{-2}	8.0×10^{-3}	5.0×10^{-3}
06/05/2021	D_{12}	82	432	---	3.5×10^{-4}	2.9×10^{-2}	1.2×10^{-2}	2.3×10^{-2}
08/02/2022	D_{13}	81	555	1270	7.1×10^{-4}	5.8×10^{-2}	4.0×10^{-3}	4.0×10^{-3}
09/02/2022	D_{14}	78	756	1450	8.5×10^{-4}	7.0×10^{-2}	4.0×10^{-3}	5.0×10^{-3}
10/02/2022	D_{15}	75	600	---	8.4×10^{-4}	6.9×10^{-2}	1.0×10^{-2}	5.0×10^{-3}
14/02/2023	D_{16}	83	661	---	6.0×10^{-4}	4.9×10^{-2}	4.0×10^{-3}	1.5×10^{-2}
07/09/2023	AS_4	81	779	---	6.3×10^{-3}	5.2×10^{-1}	9.8×10^{-4}	---
08/09/2023	AS_5	83	430	---	2.0×10^{-3}	1.7×10^{-1}	1.2×10^{-3}	---
Average dust							$9\ (\pm 5) \times 10^{-3}$	$9\ (\pm 7) \times 10^{-3}$

Average **AS**	1.1 ($\pm$ 0.2) $\times 10^{-4}$

The average uptake coefficients for glyoxal on the Gobi mineral dust calculated at 80% RH from the gas-phase uptake and the particle formation are $\gamma_{Gly\text{-}Dust\text{-}gas}$ = 9 × 10^{-3} (standard deviation ± 5) and $\gamma_{Gly\text{-}Dust\text{-}OA}$ = 9 × 10^{-3} (standard deviation ± 7), respectively. The two average values agree. This suggests that every glyoxal molecule in the gas phase is taken up by the airborne dust particles. This suggests also that the uptake occurs on airborne particles only, as expected as the dust particles are selected in the submicron range and that minimal deposition of dust particles is observed in the first 30 minutes after injection. The primary mechanism of particle loss during this period is dilution, which does not interfere with uptake. The standard deviations of the mean values are large, being attributed to the fact that the state of the chamber walls and the dust size distribution vary from one experiment to the other, and that the aerosol/chamber walls surface ratio is very low (0.08-1.5 × 10^{-3}). The presence of ozone appears uninfluential.

3.3. Evidence of irreversible particle growth

Figure 1 shows that, even in the more favourable conditions (RH=80%), the ratio between the observed increase of the POM (2 µg m^{-3}) and that of the particle volume concentration (20 µm^3 cm^{-3}) corresponds to an estimated mass density of the order of 0.1 g cm^{-3}, which is about 10 times lower than the value of 1 g cm^{-3} expected for glyoxal. This is partially attributed to the fact that only part of the organic matter formed on dust is detected by the ACSM. On the other hand, **Figure S3** shows that, after reaching its maximum value, the volume concentration decreases at a lower rate than the POM (slope 3.9 × 10^{-5} s^{-1} and 6.1 × 10^{-5} s^{-1}, respectively). This suggests that an additional process could contribute the particle volume concentration partially compensating the loss of organic matter on the dust particles.

This is confirmed by **Figure 4,** which shows the variation in time of the normalised particle volume distributions, at four steps of the experiments performed at 30% RH and 80% RH. Those include prior and glyoxal injection, POM maximum peak value, and the end of the experiment.

501

502
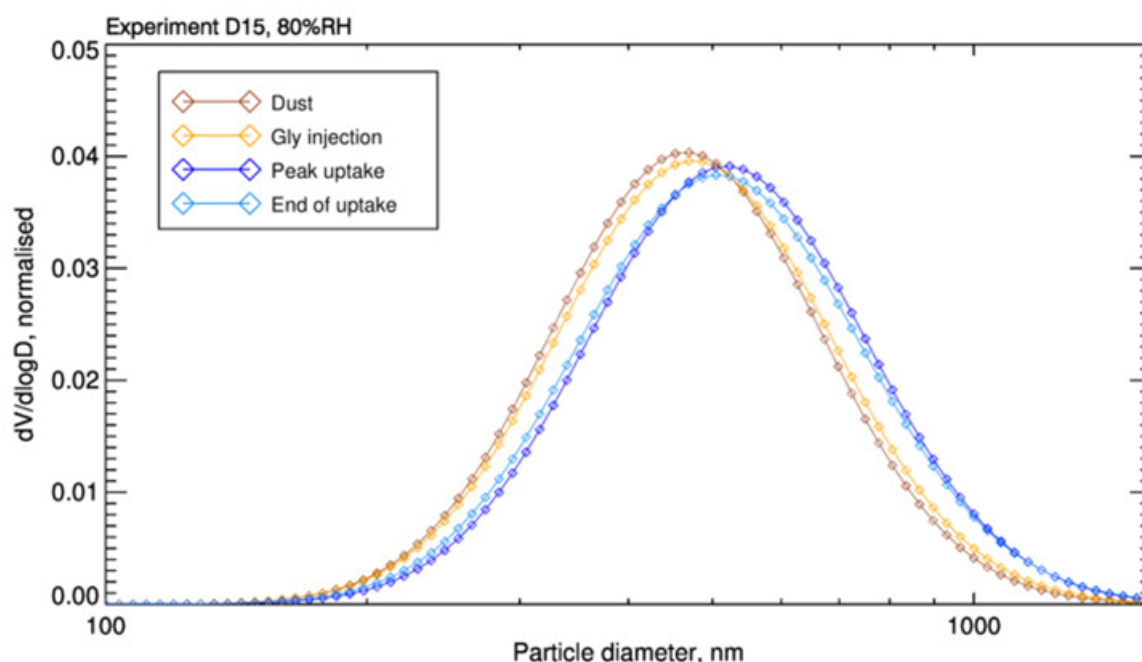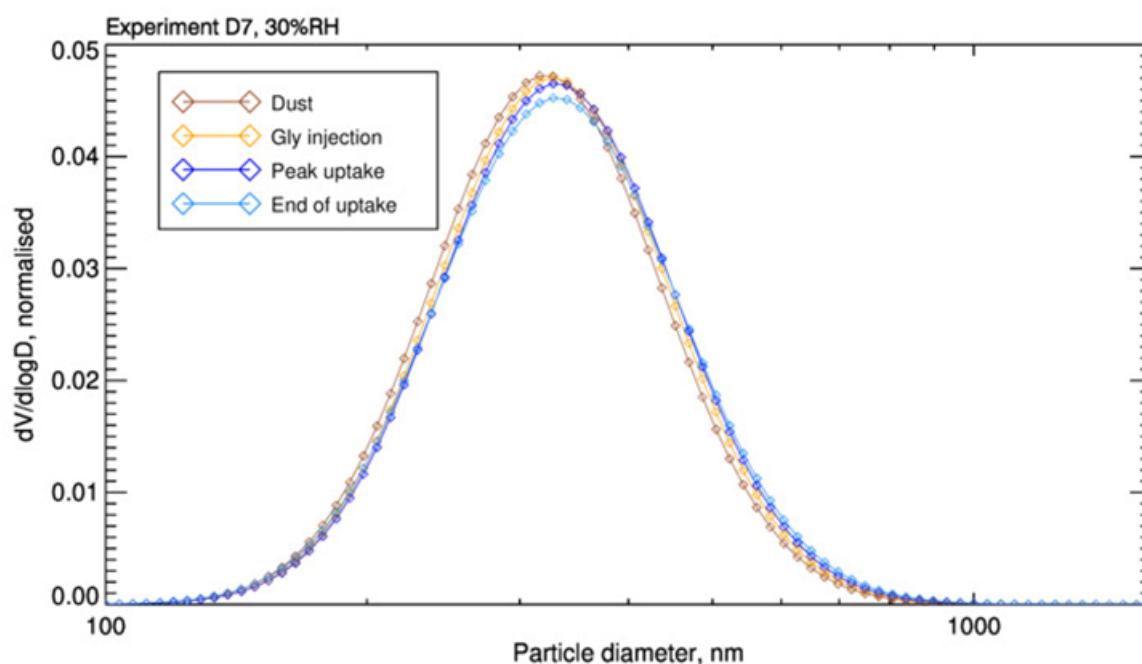
Figure 4. Evolution of volume-size distributions for two glyoxal uptake experiments in different relative humidity conditions. The images illustrate the progression of volume-size distributions recorded at four key moments during the experiments. The first distribution (orange) is recorded after the dust is injected into the simulation chamber. The second distribution (yellow) is recorded at the moment of glyoxal injection. The third distribution (blue) corresponds to the peak uptake of glyoxal on the aerosol, and the fourth (light blue) is recorded at the end of glyoxal uptake process. The left image depicts the evolution for the experiment D7 conducted at 30% RH, while the image on the right shows the distributions for the experiment D15 conducted at 80% RH. The results highlight that the distributions grow more significantly at 80% RH, indicating a higher glyoxal uptake and organic formation at elevated humidity levels.

513   All distributions have a single mode. However, after the injection of glyoxal, the

514   geometric mean volume diameter, measured at the maximum POM concentration,

increases by up to 10% (from 310 to 340 nm) at 30% RH, and up to 20% (from 450 to 540 nm) at 80% RH. Interestingly, even at the end of the experiment, when the POM concentration returns to its initial value, the increase in geometric mean diameter of the aerosol is irreversible. We hypothesize that the uptake of glyoxal enhances the dust hygroscopicity Therefore the difference in total volume between the beginning and end of the experiment is due to formed organic aerosol mass, resulting from water uptate.

3.4. Chemical composition of the particulate organic matter

This section discusses the chemical composition of the particulate organic matter formed on the mineral dust following the interaction with glyoxal. The list and conditions of the filter samples analysed by SFE/GC-MS and ESI-Orbitrap are reported in **Table S2** in the Supplementary Material. Details of the organic composition of the native dust are provided in **Text S6**.

3.4.1. Timeline of chemical evolution

Figure 5 shows the time evolution of the intensity of the organic fragments detected by the ToF-ACSM at 80% RH (experiment D_{15}) at four moments of the experiment: 1) before the injection of glyoxal; 2) during the uptake and the formation of the organic matter; 3) after the organic matter has reached its maximum concentration; and 4) at the end of the experiment, when the organic matter returned to its initial concentration.

534
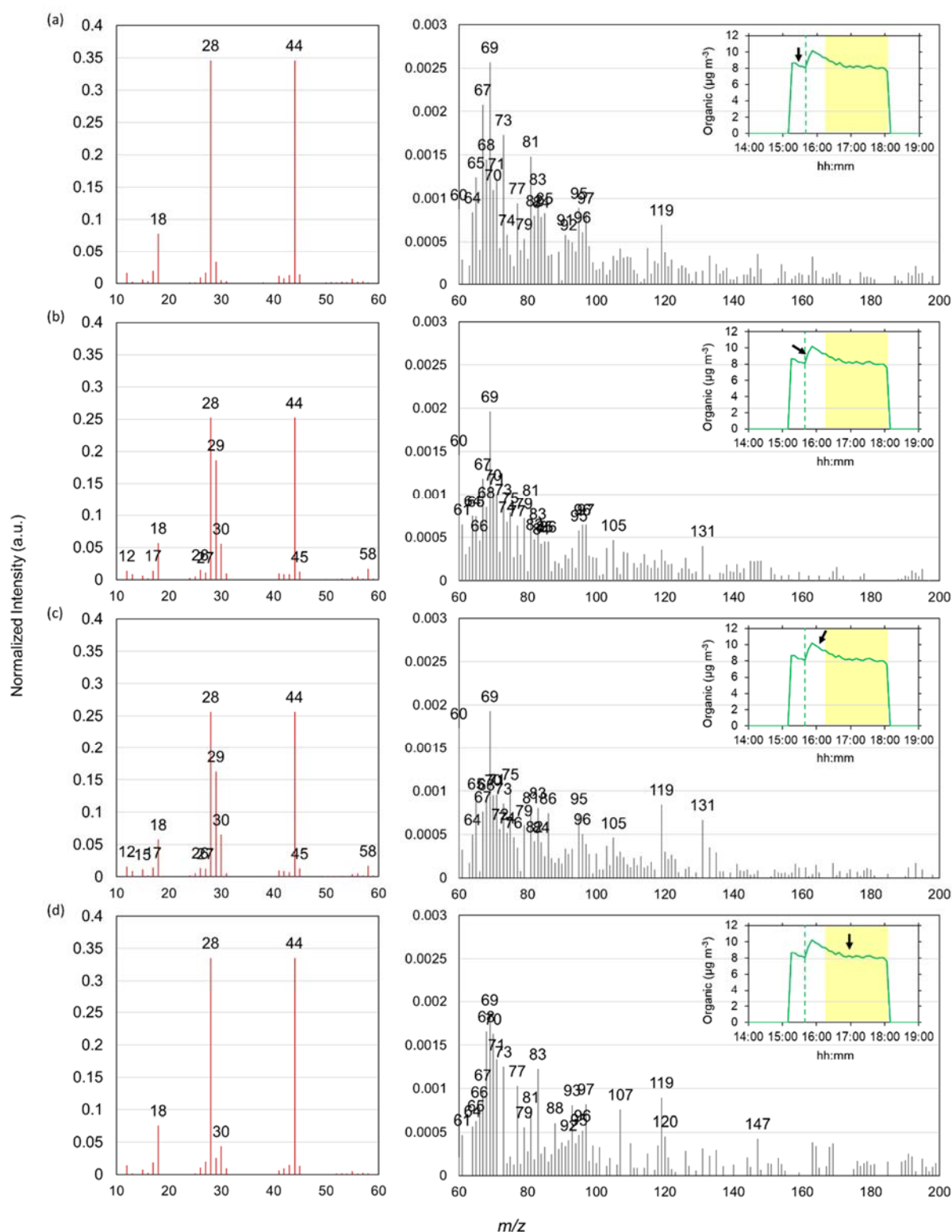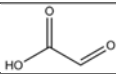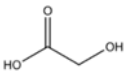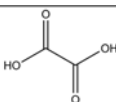
Figure 2. ACSM organic mass spectra (intensities normalized to the total organic concentration) recorded during the experiment D_{15}: (a) before glyoxal uptake (dust organic fraction composition), (b) during glyoxal uptake, (c) after reaching the maximum uptake on the particles and (d) 1h later under irradiation. Panels on the left show the mass spectra ranging from m/z 10 to 60, while the panels on the right represent fragments from m/z 60 to 200 (their intensity is approximately one hundred times lower). The inserts display the time series of organic concentrations measured by the ToF-ACSM. A black arrow indicates the time corresponding to the mass spectrum shown. The yellow-highlighted shaded area indicates the interval where irradiation takes place, while the green vertical dashed lines indicate the moment of glyoxal injection in the chamber.
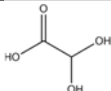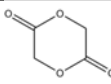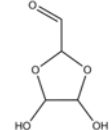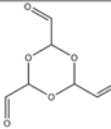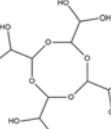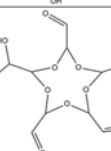
543 **Figure 5** reveals that the organic matter formed as a result of the interaction between
544 mineral dust and glyoxal is composed of oxidized organic fragments, organic acids,
545 oligomers. Oxidized organic fragments such as CO^+ (m/z 28) and CO_2^+ (m/z 44) are
546 observed through all phases of experiments. Fragments such as CHO^+ (m/z 29),
547 CH_2O^+ (m/z 30), and $C_2H_2O_2^+$ (m/z 58), appear during the uptake of glyoxal, but
548 diminish over time, due to oligomerization or further oxidation processes. The most
549 intense fragment above m/z 60 is m/z 69, which appears unrelated to glyoxal reactivity
550 but could be attributed to nitrogen-containing organic species such as $C_3H_3NO^+$,
551 originating from glyoxal–ammonia reactions (Galloway et al., 2009) or plant and soil
552 residues (Sun et al., 2010; Nieder et al., 2018). Fragments at m/z 105 and 131,
553 observed consistently during the uptake and the photolysis, could be attributed to
554 condensed glyoxal hydrates (Liggio et al., 2005; Carlton et al., 2007). Fragments at
555 m/z 119 and 120, associated with oxidized products from isoprene-derived aerosols
556 (Safi Shalamzari et al., 2013), increased after glyoxal uptake and under irradiation,
557 suggesting formation of oxidized oligomers. Upon irradiation, the appearance of m/z
558 147 and 165 – products of aqueous glyoxal oxidation and oligomer condensation (Lim
559 et al., 2010) – suggests photo-chemically enhanced transformation, though their
560 presence in native dust also points to reversible adsorption processes.

561 **3.4.2. Molecular identification**
562 The list and conditions of the samples analysed by SFE/GC-MS and ESI-Orbitrap are
563 reported in **Text S7** in the Supplementary Material, which also provides with examples
564 of analysis. The summary of the organic molecules detected by those analysis is
565 presented in **Table 3**.

566

567 **Table 3.** Summary of observed compounds identified by SFE/GC-MS analysis and glyoxal-related
568 formulas observed with ESI-Orbitrap, along with the suggested structures under the different
569 experimental conditions tested.

Molecular formula	Name	Tentative Structure	Technique	Experimental conditions
$C_2H_2O_3$	Glyoxylic acid		ESI-Orbitrap	Dust+Gly, 80%, Dark, O_3
$C_2H_4O_3$	Glycolic acid		ESI-Orbitrap SFE/GC-MS	Dust+Gly, 30%, Dark Dust+Gly, 30%, Light Dust+Gly, 80%, Light Dust+Gly, 80%, Light, O_3
$C_2H_2O_4$	Oxalic acid		ESI-Orbitrap	Dust+Gly, 80%, Light

Formula	Name	Structure	Method	Conditions
$C_2H_4O_4$	Glyoxylic acid monohydrate		ESI-Orbitrap SFE/GC-MS	Dust+Gly, 80%, Light
$C_4H_4O_4$	Glycolic acid dimer		ESI-Orbitrap	Dust+Gly, 80%, Light
$C_4H_6O_5$	Glyoxal oligomer		ESI-Orbitrap	Dust+Gly, 80%, Light
$C_6H_6O_6$	Glyoxal oligomer		ESI-Orbitrap	Dust+Gly, 80%, Light
$C_8H_{16}O_{12}$	Glyoxal oligomer		ESI-Orbitrap	Dust+Gly, 80%, Light
$C_{10}H_{12}O_{11}$	Glyoxal oligomer		ESI-Orbitrap	Dust+Gly, 80%, Dark

570

Oxidized organic compounds such as glycolic acid ($C_2H_4O_3$), oxalic acid ($C_2H_2O_4$), and a possible dimer of glycolic acid ($C_4H_4O_4$) were mainly observed under irradiated conditions, while their hydrated forms also appeared in dark conditions. Glyoxylic acid was detected in dark conditions in the presence of ozone. Glycolic and glyoxylic acids consistently form under humid conditions, indicating that their pathways may be less sensitive to water competition or that their precursors interact more strongly with dust surfaces. Light but also ozone tends to favor the formation of glycolic acid from glyoxal at high RH (**Figure S7.1**), suggesting two possible oxidative pathways. Glycolic acid is also detected at 30% RH (not showed), with and without irradiation, in agreement with the experiments on dust by Shen et al. (2016), but differently than reported by Galloway et al. (2009) on ammonium sulphate. Monohydrated glyoxylic acid is found in one sample at 80% RH under irradiated conditions, likely due to the known pattern of oxidation of glyoxal and glycolic acid with OH radicals (Buxton et al., 1997). Unlike previous studies (Galloway et al., 2009; Rubasinghege et al., 2013; Shen et al., 2016), formic acid was not detected, possibly due to high RH suppressing its formation by limiting access to reactive surface sites, as suggested by Shen et al. (2016).

Oligomerization products (compounds from C4 to C10) of the glyoxal mono- and di-hydrate forms, are observed only at 80% RH. These are: $C_4H_6O_5$ (1 monohydrated glyoxal + 1 dehydrated glyoxal forming a 5-atom ring), $C_8H_{16}O_{12}$ (4 dehydrated glyoxal

590 molecules forming an 8-membered ring), and $C_{10}H_{12}O_{11}$ (4 monohydrated glyoxal

591 molecules + 1 dehydrated glyoxal molecule forming a ring structure). The oligomer

592 $C_6H_6O_6$ (3 molecules of monohydrated glyoxal forming a 6-membered ring) is detected

593 only under dark conditions. $C_8H_{16}O_{12}$, can correspond to an oligomer previously

594 observed by Shen et al. (2016) on mineral dust.

595 The persistence of low-volatility, heavy compounds, such as oligomers at the surface

596 of mineral dust has implications for its oxidation state, which is modified in an

597 irreversible way its surface composition, as already shown by previous studies on

598 ammonium sulphate seeds (Kroll et al., 2005; Galloway et al., 2009; De Haan et al.,

599 2020; Hu et al., 2022). This is illustrated by the van Krevelen diagrams obtained from

600 the ESI-Orbitrap analysis in **Figure 6**.

601
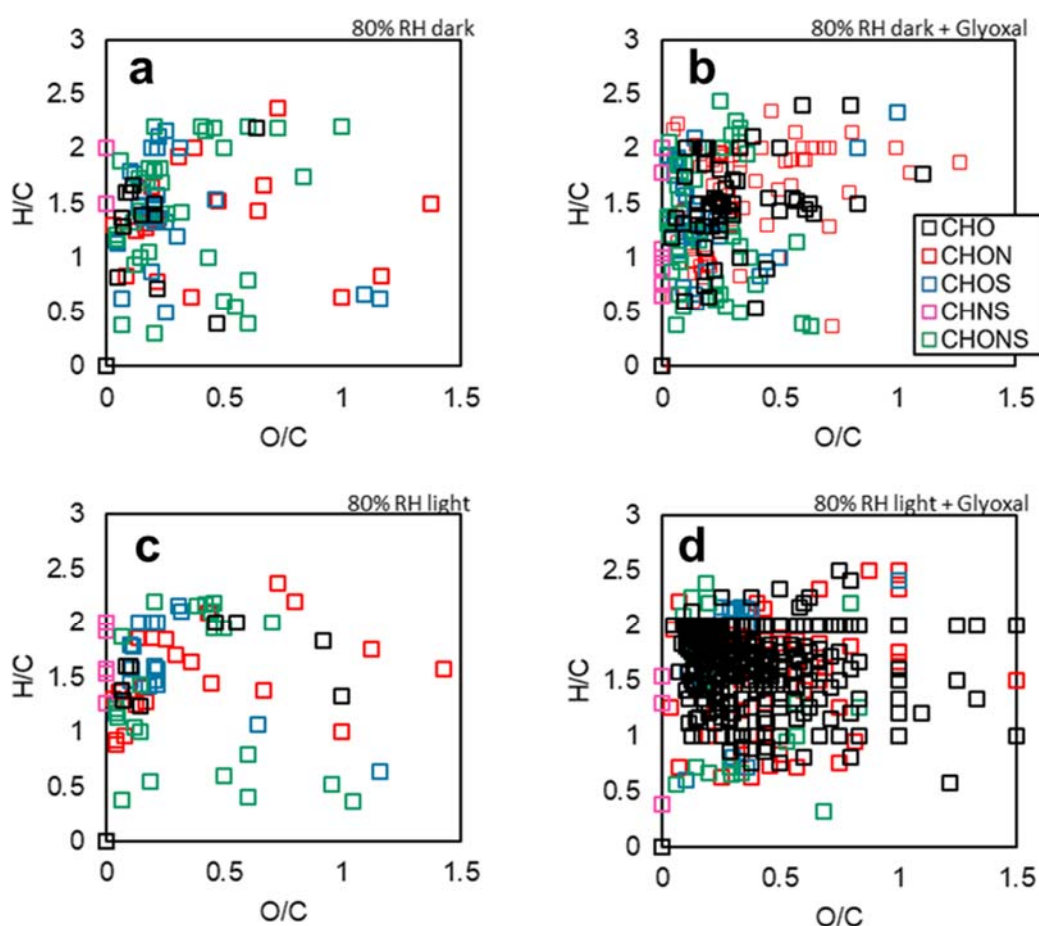
602 **Figure 6.** Van Krevelen diagrams recorded at 80% RH for: in the top line experiments in the dark for
603 mineral dust only (control experiment D_2, left) and one ageing experiment of dust with glyoxal
604 (experiment D10); bottom line: same with irradiation. Samples are equivalent in terms of load of
605 particulate organic matter. These are 0.9 µg (sample a), 0.8 µg (sample b), 1.7 µg (sample c) and 0.6
606 µg (sample d). Despite an equivalent loading of particulate organic mass, the number of signals detected
607 is significantly higher when the dust is exposed to glyoxal (86 and 102 peaks detected for dust only
608 against 398 and 310 with glyoxal, and with and without light, respectively).

609

The processing by the glyoxal clearly has an effect on the oxidation state of the dust, particularly when lights are on, resulting in the appearance of signals with O/C ratio higher than 1, attributed to photo-oxidation. The predominant family in this case is that of CHO molecules, while the appearance of molecules for families CHON and CHONS is also observed.

4. Discussion

4.1. Comparison of uptake coefficients

The uptake of glyoxal on the dust particles occurs in humid conditions exceeding 30% RH. These observations agree with the results of Liggio et al. (2005a; 2005b) on the uptake of glyoxal on ammonium sulphate aerosols, observing the formation of organic matter only when RH exceeded 50%. Trainic et al. (2011) also observed that the uptake of glyoxal on glycine and ammonium sulphate particles occurred only when the relative humidity was above 35%. On the contrary, both Shen et al (2016) and Zogka et al. (2024) demonstrated that the uptake can occur in dry conditions too, which was not observed in this work.

At 80% RH, the experimental-average of the measured uptake coefficient of glyoxal on mineral dust is $\gamma = (9 \pm 5) \times 10^{-3}$. Our values are approximately one order of magnitude higher than those obtained by Shen et al. (2016) who investigated the uptake of glyoxal on mineral proxies, i.e. SiO_2, and $CaCO_3$ and $\alpha\text{-}Al_2O_3$ under various levels of RH. These authors determined the uptake coefficients after a long exposition of the surface to glyoxal (steady state uptakes) and found that the uptake coefficients decrease with increasing the gas phase concentration of glyoxal. At 1 ppb concentration and 60% RH, the uptake coefficient determined on suspended particles of calcite ($CaCO_3$) is $1.4 (\pm 0.1) \times 10^{-4}$ and $5.5 \pm (0.1) \times 10^{-5}$ on alumina ($\alpha\text{-}Al_2O_3AlO_3$).

Zogka et al. (2024) used a Knudsen cell to evaluate the initial and steady state glyoxal uptake coefficient bulk soil samples of various origins. At low RH, these authors found that for Gobi soil sieved to less than 63 μm in diameter, the initial uptake coefficient using the geometric surface area was 0.18 (corresponding to an upper limit of the uptake), independent of glyoxal concentration. However, the steady state uptake coefficients determined after a long processing of surface were found to decrease with increasing glyoxal concentration, due to aging of the surface.

641   Various reasons could induce those apparent differences. First, the differences in the

642   experimental set up. In CESAM the initial uptake coefficient was measured on dust

643   aerosol particles in suspension in a large volume, compared to sieved soil (Zogka et

644   al., 2024) and grinded mineral powders (Shen et al., 2016). The uptake coefficient is

645   inversely proportional to the available particle surface. In our experiments, the dust

646   available geometric surface density, calculated from the measured size distribution

647   assuming spherical particles, is in the range 0.35-6.3 × 10^{-3} m² m⁻³ (**Table 2**). As the

648   the CESAM chamber volume is equal to 4.2 m³, the total dust surface area available

649   for the reaction ranges from 2 to 2.6 × 10^{-3} m², several orders of magnitude lower than

650   in the experiments designed by Shen et al. (2016) and Zogka et al. (2024). Shen et al.

651   (2016) used model powders of various sizes between 35 nm and 5 µm, with BET

652   (define BET) surface areas ranging between 1.4 and 440 m² g⁻¹. In the conservative

653   assumption that only 5 mg of the model powder was used, the total reactive surface

654   area was up to 2.2 m². Zogka et al. (2024) used the soil from Gobi sieved to 63 µm

655   and a BET surface area of 10.5 ± 1.0 m² g⁻¹. Using even just 1 g would yield a surface

656   area of the order of 10.5 m². Differences in the results could also arise by differences

657   in the dust mineralogy, which are difficult to ascertain in the present study.

658   Our estimated uptake coefficient of glyoxal on mineral dust is also nearly two orders of

659   magnitude higher than for ammonium sulphate (γ_{gas-AS} = 1.1 (± 0.2) × 10^{-4}; our study

660   as well as Curry et al., 2018; De Haan et al., 2020; Galloway et al., 2009; Liggio et al.,

661   2005b, a; Trainic et al., 2011), but lower than γ_{gas-AS} = 2.9 × 10^{-3} at a lower RH (Liggio

662   et al., 2005). The difference could be due to the higher hygroscopicity of ammonium

663   sulphate, enhancing water's competition with glyoxal for adsorption sites at 80% RH,

664   when indeed ammonium sulphate is deliquescent. This suggest nonetheless that dust

665   aerosols could play a very substantial role in the formation of organic aerosols at high

666   RHcompared to ammonium sulphate, which is often used as an aerosol proxy.

667   **4.2. Mechanism of chemical transformation**

668   **Figure 7** illustrates the suggested chemical mechanisms of the transformation of gas-

669   phase glyoxal on the mineral dust particles.

670

671
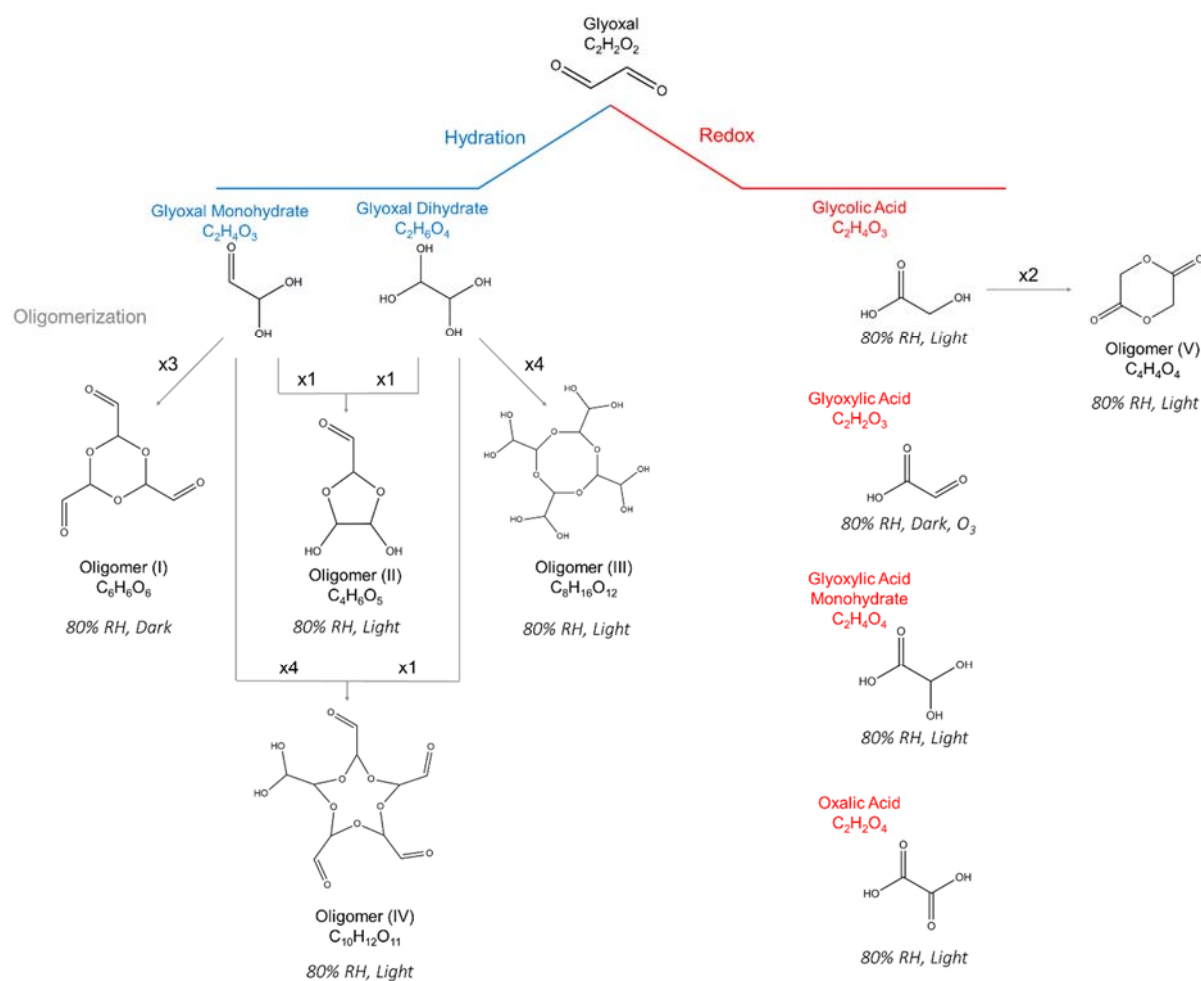
Figure 7. Proposed reaction scheme to explain the glyoxal-related molecular formulas detected through ESI-Orbitrap mass spectrometry and SFE/GC-MS.

The multiphase chemistry of glyoxal on mineral dust particles, leading to the formation of low-volatility, particle-phase products, is complex, involving hydration, redox, and oligomerization pathways. The chemical transformation of glyoxal upon uptake by mineral dust particles primarily occurs through aqueous-phase reactions. The mechanism is initiated by hydration of glyoxal's aldehyde groups, forming mono- and di-hydrated species. These hydrated intermediates undergo condensation reactions, which involve nucleophilic attack and lead to the formation of cyclic acetal structures, particularly from two to five-membered dioxolane rings. This mechanism is well supported by prior studies (Loeffler et al., 2006; Kua et al., 2008; Hastings et al., 2005), which have described similar pathways for glyoxal oligomerization in aqueous environments.

This study provides new insight into how this chemistry on mineral surfaces. While previous research has shown that glyoxal typically forms dimers and trimers in aqueous solution (Liggio et al., 2005; Nozière et al., 2009), our mass spectral data reveal the presence of oligomeric species containing up to 5 glyoxal units. This higher degree of oligomerization - also observed by Shen et al. (2016) - suggests that the particle-phase environment allows for extended oligomer growth. The likely contributing factors include reduced water activity, surface confinement, and enhanced proximity of reactants, all of which promote successive addition reactions that may be hindered in bulk solution (Gomez et al., 2015; Avzianova & Brooks, 2013).

Redox reactions derive into oxidized species such as glycolic, glyoxylic, and oxalic acids. These compounds not only represent aging products but also participate in further condensation reactions, expanding the chemical diversity of SOA. In particular, we detected the presence of oligomer V, which we propose results not from direct glyoxal self-reactions but rather from the condensation of two glycolic acid molecules. This suggests a broader heterogeneous transformation process occurring on the dust surface, possibly involving oxidative pathways. Such cross-reactions are consistent with mechanisms proposed in glyoxal–methylglyoxal systems (Zhang et al., 2022), where mixed oligomers form through shared reaction intermediates.

A key aspect of our findings is the irreversibility of glyoxal uptake on mineral dust. In contrast to bulk aqueous systems, where glyoxal oligomerization can exist in equilibrium with monomeric species, our results suggest that oligomer formation on mineral particles is effectively irreversible. The persistence of high-molecular-weight products following drying and thermal analysis confirms that these species are chemically stable and remain in the condensed phase. This behaviour is consistent with previous observations (Hastings et al., 2005; Ortiz-Montalvo et al., 2014), and highlights the significance of particle-phase reactions in the formation of SOA.

The acidity of the particle surface could potentially play a role in catalysing glyoxal oligomerization. It is plausible that localized acidity arises or is enhanced by the accumulation of transformation products such as glycolic and oxalic acids, which were detected in this study. This in-situ acidification may facilitate acid-catalysed reaction pathways even under neutral or weakly acidic conditions. The importance of acidity in glyoxal chemistry is supported by mechanistic proposals involving carbenium ion intermediates or hydrogen-bond-assisted nucleophilic mechanisms, which can operate

effectively without requiring strongly acidic environments (Zhang et al., 2022; Gomez et al., 2015). These pathways are known to promote the formation of low-volatility oligomers, contributing to organic aerosol mass. Similarly, Ortiz-Montalvo et al. (2014) demonstrated that even mildly acidic aerosols significantly enhance glyoxal oligomerization and SOAformation.

Another critical factor is the presence of adsorbed water on mineral dust particles. Our findings demonstrate in fact that the availability of surface water facilitates organic aerosol formation from glyoxal. This agrees with chamber and field studies (Hastings et al., 2005; Shen et al., 2016) that identified a RH threshold above which glyoxal uptake dramatically increases. The presence of a thin aqueous film on the particle surface creates a reactive medium where glyoxal can concentrate, hydrate, and polymerize efficiently. Even after evaporation, the products formed are retained in the particle phase, evidencing their low volatility and chemical resilience.

4.3. Implications for the dust properties

The irreversible transformation of the chemical composition of mineral dust following the uptake of glyoxal could influence the physico-chemical properties of mineral dust particles. The formation of organic acids (glycolic, glyoxylic and oxalic acids) should change the dust pH, increasing its acidity and ability to dissolve transition metals like iron and copper. This could alter their speciation, enhancing their bioavailability in aqueous aerosol environments and potentially impacting atmospheric chemistry and the reactivity of aerosol particles (Giorio et al., 2022). Changes in dust pH could also affect its hygroscopic properties, influencing their ability to adsorb water and grow in size. This is consistent with our observation regarding the volume increase of dust particles after the uptake and the subsequent growth that enhance particles interaction with light and cloud droplets formation. Collectively, these processes highlight how aerosol acidity modulates not only chemical transformations but also key physical properties and atmospheric lifetimes of dust-glyoxal systems.

The newly formed organic matter from glyoxal on dust particles could also alter the aerosol's optical properties, affecting its ability to absorb solar radiation, as recently observed in aqueous solution (De Haan et al., 2023) or on ammonium sulphate aerosols (De Haan et al. 2020; Trainic et al. 2011). The presence of hydrated glyoxal oligomeric structures has already been observed to have UV radiation absorption properties (Kalberer et al., 2004; Shapiro et al., 2009). Glyoxal-derived oligomers could

significantly influence the optical properties of mineral dust aerosols. Spectroscopic analyses revealed that these oligomers have broadened OH and C–O bands and enhanced Raman activity, indicative of their hydrated and cyclic structures (Avzianova and Brooks, 2013). They also have strong UV-visible absorption, particularly between 300–600 nm, with characteristic shoulders at ~280 and 345 nm attributed to acetal and aldol condensation products (Schwier et al., 2010; Shapiro et al., 2009). High RH conditions (> 80%) facilitate brown carbon formation, evidenced by the further appearance of UV-visible absorbance peaks and Raman background signals (De Haan et al., 2020; Zhang et al., 2022).

5. Conclusions

This paper presented a novel investigation of the interaction between gas-phase glyoxal and mineral dust. By taking advantage of the capabilities of the CESAM atmospheric simulation chamber to perform multiphase experiments on time scales relevant to atmospheric processes and dispersion, including aerosols, our experiments considered airborne submicron mineral dust particles generated from a natural soil (Gobi Desert) in realistic concentrations, composition and size distribution. While airborne, the dust aerosol was aged under variable conditions ofRH, irradiation, and ozone concentrations. Thanks to the realism of the tools and the experimental conditions, our study investigates, for the first time, both the rate of uptake of glyoxal and the rate of formation of the organic aerosol from the gas-phase uptake. We provide the chemical composition of the particle formed on the dust particles, and their implications on the particle microphysics, in atmospheric-relevant conditions.

This study used a single and instantaneous injection of glyoxal, and not a constant steady state flux. Above 30% RH, upon injection, glyoxal is partitioned almost instantaneously between the gas phase, the chamber walls and the dust particles. This is an advantage to scale our results to ambient conditions. Indeed, Volkamer et al. (2005) estimated that the daytime lifetime of glyoxal is around 1.3 h. Alvarado et al. (2020) showed that the long-range transport of glyoxal produced from a point source (Canadian wildfires) may be possible only by invoking the progressive oxidation of its longer-lived precursors in the plume. In the scenario where dust aerosols interact with a glyoxal plume from a point source, one can expect an interaction time of a few minutes, compatible with that of this study. Furthermore, because the uptake follows a

784   first order kinetic, the measured uptake coefficient ($\gamma = (9 \pm 5) \times 10^{-3}$ at 80% RH) is

785   independent of the glyoxal concentration and transferable to atmospheric conditions.

786   The uptake of glyoxal and the formation of organic matter start as soon as the glyoxal

787   is injected in the chamber and last approximately 20 minutes. The uptake coefficient

788   measured by the loss of gas-phase glyoxal molecules agrees very well with the rate of

789   formation of the particulate organic mass on the dust, suggesting that the totality of the

790   mass of reacting glyoxal is condensed on the dust particles. While some of the organic

791   matter is lost again from the dust particles due to evaporation, oligomers and organic

792   acids are detected on the dust even after the uptake has finished, indicating that the

793   uptake of glyoxal modifies irreversibly both the composition and the physical properties

794   of mineral dust.

795   This study reveals a significant quantitative transfer of gas-phase glyoxal molecules to

796   mineral dust aerosol surfaces, occurring within a timescale of a few minutes,

797   underscoring the important role of dust-glyoxal interactions in the atmosphere. Our

798   results extend the current understanding of glyoxal chemistry in atmospheric systems.

799   While oligomerization occurs through well-established aqueous-phase pathways, we

800   suggest that mineral dust particles facilitate in a unique way higher-order oligomer

801   formation, support irreversible uptake, and possibly promote alternative reaction

802   channels such as glycolic acid condensation. These findings underscore the

803   importance of mineral dust surfaces as active sites for multiphase SOA formation, with

804   implications for understanding aerosol growth, composition, and climate-relevant

805   properties. This is also in agreement with the field observations conducted by Wang et

806   al. (2015). Neglecting the uptake pathway on dust could result in an underestimation

807   of glyoxal removal from the atmosphere, potentially leading to disparities between

808   model predictions and observed gaseous concentrations of glyoxal (Kluge et al., 2023;

809   Ling et al., 2020; Volkamer et al., 2007; Washenfelder et al., 2011).The findings of this

810   study have also important implications for the aerosol direct and indirect radiative effect

811   and aerosol pH. The acidification and the oxidation of the dust aerosols by glyoxal

812   should increase their hygroscopicity, especially under high RH conditions, affecting

813   particle growth dynamics, phase behaviour, and cloud condensation nuclei (CCN)

814   potential (Song and Osada, 2021). Further data analysis are ongoing to address these

815   aspects.

816

Data availability. The simulation chamber experiments that support the findings of this study are available through the Database of Atmospheric Simulation Chamber Studies (DASCS) of the EUROCHAMP Data Centre (https:// data.eurochamp.org/ data- access/ chamber- experiments/).

Code availability. The routine used for fitting the size distribution is available at https://doi.org/10.5281/zenodo.8135133 (Baldo and Lu, 2023). Note that in this study we only used the size distribution measured by the OPC instrument, which was fitted with a lognormal function. The Tof-ACSM data processing (including mass calibration, peaks integration and air beam correction of ion intensities) was conducted with Tofware version 3_2_40209, the ACSM data analysis package for the software Igor Pro 7.08 (Wavemetrics, Inc., Portland, OR, USA). SFE-GC-MS data analysis was conducted using the proprietary software (TurboMass Version 6.1.0.1965 PerkinElmer®).

Author contributions. PF, JFD and FB conceptualized the study. PF and FB led the paper writing, with contributions from all the authors. JFD provided with expertise on multi-phase chemistry. CB analysed the aerosol size distribution data. VM supervised the analysis of PTR-MS data. FB, CG and DLP performed the ESI-Orbitrap analysis of filter samples. FB and JFB performed the analysis of ACSM observations. FB, TB and AG performed the SFE/CG-MS analysis of filter samples. FB, GN and SC performed the thermo-optical analysis of filter samples. FB, MC, AB, EP, VM, BPV and PF conducted the chamber experiments. MR provided with the soil sample and expertise on heterogeneous chemistry. PF provided with funding.

Competing interests. The authors declare no competing interests.

Special issue statement. This article is not part of a special issue. It is not associated with a conference.

Acknowledgements. The AERIS data center (www.aeris–data.fr) is acknowledged for distributing and curing the data produced by the CESAM chamber through the hosting of the EUROCHAMP data center (https://data.eurochamp.org). The initial contribution of M. Giordano (Afri-SET) to the conceptualisation of the project is gratefully acknowledged. The authors wish to thank the two anonymous referees for helping to improve the manuscript.

Financial support. This work has received funding from the French National Research Agency (ANR) though the research project CLIMDO under the grant number ANR-19-CE01-0008-02. It has received support from the European Union's Horizon 2020 research and innovation program through the EUROCHAMP-2020 Infrastructure Activity under grant agreement no. 730997. CNRS-INSU is gratefully acknowledged for supporting the CESAM chamber as a national facility as part of the French ACTRIS Research Infrastructure.

References

Adebiyi, A., Kok, J. F., Murray, B. J., Ryder, C. L., Stuut, J.-B. W., Kahn, R. A., Knippertz, P., Formenti, P., Mahowald, N. M., Pérez García-Pando, C., Klose, M., Ansmann, A., Samset, B. H., Ito, A., Balkanski, Y., Di Biagio, C., Romanias, M. N., Huang, Y., and Meng, J.: A review of coarse mineral dust in the Earth system, Aeolian Research, 60, 100849, https://doi.org/10.1016/j.aeolia.2022.100849, 2023.

Aiken, A. C., DeCarlo, P. F., Kroll, J. H., Worsnop, D. R., Huffman, J. A., Docherty, K. S., Ulbrich, I. M., Mohr, C., Kimmel, J. R., Sueper, D., Sun, Y., Zhang, Q., Trimborn, A., Northway, M., Ziemann, P. J., Canagaratna, M. R., Onasch, T. B., Alfarra, M. R., Prevot, A. S. H., Dommen, J., Duplissy, J., Metzger, A., Baltensperger, U., and Jimenez, J. L.: O/C and OM/OC Ratios of Primary, Secondary, and Ambient Organic Aerosols with High-Resolution Time-of-Flight Aerosol Mass Spectrometry, Environ. Sci. Technol., 42, 4478–4485, https://doi.org/10.1021/es703009q, 2008.

Alvarado, L. M. A., Richter, A., Vrekoussis, M., Hilboll, A., Kalisz Hedegaard, A. B., Schneising, O., and Burrows, J. P.: Unexpected long-range transport of glyoxal and formaldehyde observed from the Copernicus Sentinel-5 Precursor satellite during the 2018 Canadian wildfires, Atmos. Chem. Phys., 20, 2057–2072, https://doi.org/10.5194/acp-20-2057-2020, 2020.

Atkinson, J. D., Murray, B. J., Woodhouse, M. T., Whale, T. F., Baustian, K. J., Carslaw, K. S., Dobbie, S., O'Sullivan, D., and Malkin, T. L.: The importance of feldspar for ice nucleation by mineral dust in mixed-phase clouds, Nature, 498, 355–358, https://doi.org/10.1038/nature12278, 2013.

Avzianova, E. and Brooks, S. D.: Raman spectroscopy of glyoxal oligomers in aqueous solutions, Spectrochimica Acta Part A: Molecular and Biomolecular Spectroscopy, 101, 40–48, https://doi.org/10.1016/j.saa.2012.09.050, 2013.

Baldo, C., Formenti, P., Di Biagio, C., Lu, G., Song, C., Cazaunau, M., Pangui, E., Doussin, J.-F., Dagsson-Waldhauserova, P., Arnalds, O., Beddows, D., MacKenzie, A. R., and Shi, Z.: Complex refractive index and single scattering albedo of Icelandic dust in the shortwave part of the spectrum, Atmos. Chem. Phys., 23, 7975–8000, https://doi.org/10.5194/acp-23-7975-2023, 2023.

Battaglia, F., Baldo, C., Cazaunau, M., Bergé, A., Pangui, E., Picquet-Varrault, B., Doussin, J.-F., and Formenti, P.: Protocol for generating realistic submicron mono-dispersed mineral dust particles in simulation chambers and laboratory experiments, Aerosol Science and Technology, 59, 357–369, https://doi.org/10.1080/02786826.2024.2442518, 2025.

Bauer, S. E., Mishchenko, M. I., Lacis, A. A., Zhang, S., Perlwitz, J., and Metzger, S. M.: Do sulfate and nitrate coatings on mineral dust have important effects on radiative properties and climate modeling?, J. Geophys. Res., 112, D06307, https://doi.org/10.1029/2005JD006977, 2007.

Brégonzio-Rozier, L., Giorio, C., Siekmann, F., Pangui, E., Morales, S. B., Temime-Roussel, B., Gratien, A., Michoud, V., Cazaunau, M., DeWitt, H. L., Tapparo, A., Monod, A., and Doussin, J.-F.: Secondary organic aerosol formation from isoprene photooxidation during cloud condensation–evaporation cycles, Atmos. Chem. Phys., 16, 1747–1760, https://doi.org/10.5194/acp-16-1747-2016, 2016.

Buxton, G. V., Malone, T. N., and Arthur Salmon, G.: Oxidation of glyoxal initiated by OH in oxygenated aqueous solution, Faraday Trans., 93, 2889–2891, https://doi.org/10.1039/a701468f, 1997.

Carlton, A. G., Turpin, B. J., Altieri, K. E., Seitzinger, S., Reff, A., Lim, H.-J., and Ervens, B.: Atmospheric oxalic acid and SOA production from glyoxal: Results of aqueous photooxidation experiments, Atmospheric Environment, 41, 7588–7602, https://doi.org/10.1016/j.atmosenv.2007.05.035, 2007.

Castellanos, P., Colarco, P., Espinosa, W. R., Guzewich, S. D., Levy, R. C., Miller, R. L., Chin, M., Kahn, R. A., Kemppinen, O., Moosmüller, H., Nowottnick, E. P., Rocha-Lima, A., Smith, M. D., Yorks, J. E., and Yu, H.: Mineral dust optical properties for remote sensing and global modeling: A review, Remote Sensing of Environment, 303, 113982, https://doi.org/10.1016/j.rse.2023.113982, 2024.

Chan, C., Jacob, D. J., Marais, E. A., Yu, K., Travis, K. R., Kim, P. S., Fisher, J. A., Zhu, L., Wolfe, G. M., Hanisco, T. F., Keutsch, F. N., Kaiser, J., Min, K.-E., Brown, S. S., Washenfelder, R. A.,

González Abad, G., and Chance, K.: Glyoxal yield from isoprene oxidation and relation to formaldehyde: chemical mechanism, constraints from SENEX aircraft observations, and interpretation of OMI satellite data, Atmos. Chem. Phys., 17, 8725–8738, https://doi.org/10.5194/acp-17-8725-2017, 2017.

Chen, S., Chen, J., Zhang, Y., Lin, J., Bi, H., Song, H., Chen, Y., Lian, L., Liu, C., and Zhang, R.: Anthropogenic dust: sources, characteristics and emissions, Environ. Res. Lett., 18, 103002, https://doi.org/10.1088/1748-9326/acf479, 2023.

Chirizzi, D.: Influence of Saharan dust outbreaks and carbon content on oxidative potential of water-soluble fractions of PM2.5 and PM10, Atmospheric Environment, 2017.

Crowley, J. N., Ammann, M., Cox, R. A., Hynes, R. G., Jenkin, M. E., Mellouki, A., Rossi, M. J., Troe, J., and Wallington, T. J.: Evaluated kinetic and photochemical data for atmospheric chemistry: Volume V – heterogeneous reactions on solid substrates, Atmos. Chem. Phys., 10, 9059–9223, https://doi.org/10.5194/acp-10-9059-2010, 2010.

De Haan, D. O., Hawkins, L. N., Jansen, K., Welsh, H. G., Pednekar, R., De Loera, A., Jimenez, N. G., Tolbert, M. A., Cazaunau, M., Gratien, A., Bergé, A., Pangui, E., Formenti, P., and Doussin, J.-F.: Glyoxal's impact on dry ammonium salts: fast and reversible surface aerosol browning, Atmos. Chem. Phys., 20, 9581–9590, https://doi.org/10.5194/acp-20-9581-2020, 2020.

De Haan, D. O., Hawkins, L. N., Wickremasinghe, P. D., Andretta, A. D., Dignum, J. R., De Haan, A. C., Welsh, H. G., Pennington, E. A., Cui, T., Surratt, J. D., Cazaunau, M., Pangui, E., and Doussin, J.-F.: Brown Carbon from Photo-Oxidation of Glyoxal and SO 2 in Aqueous Aerosol, ACS Earth Space Chem., 7, 1131–1140, https://doi.org/10.1021/acsearthspacechem.3c00035, 2023.

Denjean, C., Formenti, P., Picquet-Varrault, B., Katrib, Y., Pangui, E., Zapf, P., and Doussin, J. F.: A new experimental approach to study the hygroscopic and optical properties of aerosols: application to ammonium sulfate particles, Atmos. Meas. Tech., 7, 183–197, https://doi.org/10.5194/amt-7-183-2014, 2014.

Di Biagio, C., Formenti, P., Balkanski, Y., Caponi, L., Cazaunau, M., Pangui, E., Journet, E., Nowak, S., Caquineau, S., Andreae, M. O., Kandler, K., Saeed, T., Piketh, S., Seibert, D., Williams, E., and Doussin, J.-F.: Global scale variability of the mineral dust long-wave refractive index: a new dataset of in situ measurements for climate modeling and remote sensing, Atmos. Chem. Phys., 17, 1901–1929, https://doi.org/10.5194/acp-17-1901-2017, 2017.

Di Biagio, C., Formenti, P., Balkanski, Y., Caponi, L., Cazaunau, M., Pangui, E., Journet, E., Nowak, S., Andreae, M. O., Kandler, K., Saeed, T., Piketh, S., Seibert, D., Williams, E., and Doussin, J.-F.: Complex refractive indices and single-scattering albedo of global dust aerosols in the shortwave spectrum and relationship to size and iron content, Atmos. Chem. Phys., 19, 15503–15531, https://doi.org/10.5194/acp-19-15503-2019, 2019.

Dupart, Y., King, S. M., Nekat, B., Nowak, A., Wiedensohler, A., Herrmann, H., David, G., Thomas, B., Miffre, A., Rairoux, P., D'Anna, B., and George, C.: Mineral dust photochemistry induces nucleation events in the presence of SO 2, Proc. Natl. Acad. Sci. U.S.A., 109, 20842–20847, https://doi.org/10.1073/pnas.1212297109, 2012.

Ervens, B. and Volkamer, R.: Glyoxal processing by aerosol multiphase chemistry: towards a kinetic modeling framework of secondary organic aerosol formation in aqueous particles, Atmos. Chem. Phys., 10, 8219–8244, https://doi.org/10.5194/acp-10-8219-2010, 2010.

Fröhlich, R., Cubison, M. J., Slowik, J. G., Bukowiecki, N., Prévôt, A. S. H., Baltensperger, U., Schneider, J., Kimmel, J. R., Gonin, M., Rohner, U., Worsnop, D. R., and Jayne, J. T.: The ToF-ACSM: a portable aerosol chemical speciation monitor with TOFMS detection, Atmos. Meas. Tech., 6, 3225–3241, https://doi.org/10.5194/amt-6-3225-2013, 2013.

Fu, T.-M., Jacob, D. J., Wittrock, F., Burrows, J. P., Vrekoussis, M., and Henze, D. K.: Global budgets of atmospheric glyoxal and methylglyoxal, and implications for formation of secondary organic aerosols, J. Geophys. Res., 113, D15303, https://doi.org/10.1029/2007JD009505, 2008.

Galloway, M. M., Chhabra, P. S., Chan, A. W. H., Surratt, J. D., Flagan, R. C., Seinfeld, J. H., and Keutsch, F. N.: Glyoxal uptake on ammonium sulphate seed aerosol: reaction products and reversibility of uptake under dark and irradiated conditions, Atmos. Chem. Phys., 2009.

Giorio, C., Monod, A., Brégonzio-Rozier, L., DeWitt, H. L., Cazaunau, M., Temime-Roussel, B., Gratien, A., Michoud, V., Pangui, E., Ravier, S., Zielinski, A. T., Tapparo, A., Vermeylen, R., Claeys, M., Voisin, D., Kalberer, M., and Doussin, J.-F.: Cloud Processing of Secondary Organic Aerosol from Isoprene and Methacrolein Photooxidation, J. Phys. Chem. A, 121, 7641–7654, https://doi.org/10.1021/acs.jpca.7b05933, 2017.

Giorio, C., D'Aronco, S., Di Marco, V., Badocco, D., Battaglia, F., Soldà, L., Pastore, P., and Tapparo, A.: Emerging investigator series: aqueous-phase processing of atmospheric aerosol influences dissolution kinetics of metal ions in an urban background site in the Po Valley, Environ. Sci.: Processes Impacts, 24, 884–897, https://doi.org/10.1039/D2EM00023G, 2022.

Gomez, M. E., Lin, Y., Guo, S., & Zhang, R. (2015). Heterogeneous Chemistry of Glyoxal on Acidic Solutions. An Oligomerization Pathway for Secondary Organic Aerosol Formation. The Journal of Physical Chemistry A, 119(19), 4457–4463. https://doi.org/10.1021/jp509916r

Goodman, A. L., Underwood, G. M., and Grassian, V. H.: Heterogeneous Reaction of NO $_2$: Characterization of Gas-Phase and Adsorbed Products from the Reaction, 2NO $_2$ (g) + H $_2$ O(a) → HONO(g) + HNO $_3$ (a) on Hydrated Silica Particles, J. Phys. Chem. A, 103, 7217–7223, https://doi.org/10.1021/jp9910688, 1999.

Guo, Y., Wang, S., Zhu, J., Zhang, R., Gao, S., Saiz-Lopez, A., and Zhou, B.: Atmospheric formaldehyde, glyoxal and their relations to ozone pollution under low- and high-NOx regimes in summertime Shanghai, China, Atmospheric Research, 258, 105635, https://doi.org/10.1016/j.atmosres.2021.105635, 2021.

Harrison, S. P., Kohfeld, K. E., Roelandt, C., and Claquin, T.: The role of dust in climate changes today, at the last glacial maximum and in the future, Earth-Science Reviews, 54, 43–80, https://doi.org/10.1016/S0012-8252(01)00041-1, 2001.

Hastings, W. P., Koehler, C. A., Bailey, E. L., & De Haan, D. O. (2005). Secondary Organic Aerosol Formation by Glyoxal Hydration and Oligomer Formation: Humidity Effects and Equilibrium Shifts during Analysis. Environmental Science & Technology, 39(22), 8728–8735. https://doi.org/10.1021/es050446l

Hettiarachchi, E. and Grassian, V. H.: Heterogeneous Reactions of Phenol on Different Components of Mineral Dust Aerosol: Formation of Oxidized Organic and Nitro-Phenolic Compounds, ACS EST Air, 1, 259–272, https://doi.org/10.1021/acsestair.3c00042, 2024.

Horowitz, A., Meller, R., and Moortgat, G. K.: The UV–VIS absorption cross sections of the ⏑-dicarbonyl compounds: pyruvic acid, biacetyl and glyoxal, 2001.

Hu, J., Chen, Z., Qin, X., and Dong, P.: Reversible and irreversible gas–particle partitioning of dicarbonyl compounds observed in the real atmosphere, Atmos. Chem. Phys., 22, 6971–6987, https://doi.org/10.5194/acp-22-6971-2022, 2022.

Joshi, N., Romanias, M. N., Riffault, V., and Thevenet, F.: Investigating water adsorption onto natural mineral dust particles: Linking DRIFTS experiments and BET theory, Aeolian Research, 27, 35–45, https://doi.org/10.1016/j.aeolia.2017.06.001, 2017.

Lai, A. C. and Nazaroff, W. W.: MODELING INDOOR PARTICLE DEPOSITION FROM TURBULENT FLOW ONTO SMOOTH SURFACES, Journal of Aerosol Science, 31, 463–476, https://doi.org/10.1016/S0021-8502(99)00536-4, 2000.

Kalberer, M., Paulsen, D., Sax, M., Steinbacher, M., Dommen, J., Prevot, A. S. H., Fisseha, R., Weingartner, E., Frankevich, V., Zenobi, R., and Baltensperger, U.: Identification of Polymers as Major Components of Atmospheric Organic Aerosols, Science, 303, 1659–1662, https://doi.org/10.1126/science.1092185, 2004.

Kluge, F., Hüneke, T., Lerot, C., Rosanka, S., Rotermund, M. K., Taraborrelli, D., Weyland, B., and Pfeilsticker, K.: Airborne glyoxal measurements in the marine and continental atmosphere:

1002   comparison with TROPOMI observations and EMAC simulations, Atmos. Chem. Phys., 23, 1369–
1003   1401, https://doi.org/10.5194/acp-23-1369-2023, 2023.

1004 Knippertz, P. and Stuut, J.-B. W. (Eds.): Mineral Dust: A Key Player in the Earth System, Springer
1005   Netherlands, Dordrecht, https://doi.org/10.1007/978-94-017-8978-3, 2014.

1006 Knote, C., Hodzic, A., Jimenez, J. L., Volkamer, R., Orlando, J. J., Baidar, S., Brioude, J., Fast, J.,
1007   Gentner, D. R., Goldstein, A. H., Hayes, P. L., Knighton, W. B., Oetjen, H., Setyan, A., Stark, H.,
1008   Thalman, R., Tyndall, G., Washenfelder, R., Waxman, E., and Zhang, Q.: Simulation of semi-
1009   explicit mechanisms of SOA formation from glyoxal in aerosol in a 3-D model, Atmos. Chem.
1010   Phys., 14, 6213–6239, https://doi.org/10.5194/acp-14-6213-2014, 2014.

1011 Kok, J. F., Adebiyi, A. A., Albani, S., Balkanski, Y., Checa-Garcia, R., Chin, M., Colarco, P. R., Hamilton,
1012   D. S., Huang, Y., Ito, A., Klose, M., Li, L., Mahowald, N. M., Miller, R. L., Obiso, V., Pérez García-
1013   Pando, C., Rocha-Lima, A., and Wan, J. S.: Contribution of the world's main dust source regions
1014   to the global cycle of desert dust, Aerosols/Atmospheric Modelling/Troposphere/Physics (physical
1015   properties and processes), https://doi.org/10.5194/acp-2021-4, 2021.

1016 Kok, J. F., Storelvmo, T., Karydis, V. A., Adebiyi, A. A., Mahowald, N. M., Evan, A. T., He, C., and Leung,
1017   D. M.: Mineral dust aerosol impacts on global climate and climate change, Nat Rev Earth Environ,
1018   4, 71–86, https://doi.org/10.1038/s43017-022-00379-5, 2023.

1019 Kourtchev, I., Doussin, J.-F., Giorio, C., Mahon, B., Wilson, E. M., Maurin, N., Pangui, E., Venables, D.
1020   S., Wenger, J. C., and Kalberer, M.: Molecular composition of fresh and aged secondary organic
1021   aerosol from a mixture of biogenic volatile compounds: a high-resolution mass spectrometry
1022   study, Atmos. Chem. Phys., 15, 5683–5695, https://doi.org/10.5194/acp-15-5683-2015, 2015.

1023 Kroll, J. H., Ng, N. L., Murphy, S. M., Varutbangkul, V., Flagan, R. C., and Seinfeld, J. H.: Chamber
1024   studies of secondary organic aerosol growth by reactive uptake of simple carbonyl compounds,
1025   J. Geophys. Res., 110, 2005JD006004, https://doi.org/10.1029/2005JD006004, 2005.

1026 Kua, J., Hanley, S. W., & De Haan, D. O. (2008). Thermodynamics and Kinetics of Glyoxal Dimer
1027   Formation: A Computational Study. The Journal of Physical Chemistry A, 112(1), 66–72.
1028   https://doi.org/10.1021/jp076573g

1029 Lewis, A. C., Hopkins, J. R., Carslaw, D. C., Hamilton, J. F., Nelson, B. S., Stewart, G., Dernie, J.,
1030   Passant, N., and Murrells, T.: An increasing role for solvent emissions and implications for future
1031   measurements of volatile organic compounds, Phil. Trans. R. Soc. A., 378, 20190328,
1032   https://doi.org/10.1098/rsta.2019.0328, 2020.

1033 Li, G., Cheng, Y., Kuhn, U., Xu, R., Yang, Y., Meusel, H., Wang, Z., Ma, N., Wu, Y., Li, M., Williams, J.,
1034   Hoffmann, T., Ammann, M., Pöschl, U., Shao, M., and Su, H.: Physicochemical uptake and
1035   release of volatile organic compounds by soil in coated-wall flow tube experiments with ambient
1036   air, Atmos. Chem. Phys., 19, 2209–2232, https://doi.org/10.5194/acp-19-2209-2019, 2019.

1037 Li, L., Mahowald, N. M., Miller, R. L., Pérez García-Pando, C., Klose, M., Hamilton, D. S., Gonçalves
1038   Ageitos, M., Ginoux, P., Balkanski, Y., Green, R. O., Kalashnikova, O., Kok, J. F., Obiso, V.,
1039   Paynter, D., and Thompson, D. R.: Quantifying the range of the dust direct radiative effect due to
1040   source mineralogy uncertainty, Atmos. Chem. Phys., 21, 3973–4005, https://doi.org/10.5194/acp-
1041   21-3973-2021, 2021.

1042 Li, Q., Gong, D., Wang, H., Wang, Y., Han, S., Wu, G., Deng, S., Yu, P., Wang, W., and Wang, B.: Rapid
1043   increase in atmospheric glyoxal and methylglyoxal concentrations in Lhasa, Tibetan Plateau:
1044   Potential sources and implications, Science of The Total Environment, 824, 153782,
1045   https://doi.org/10.1016/j.scitotenv.2022.153782, 2022.

1046 Liggio, J.: Reactive uptake of glyoxal by particulate matter, J. Geophys. Res., 110, D10304,
1047   https://doi.org/10.1029/2004JD005113, 2005a.

1048 Liggio, J., Li, S.-M., and McLaren, R.: Heterogeneous Reactions of Glyoxal on Particulate Matter:
1049   Identification of Acetals and Sulfate Esters, Environ. Sci. Technol., 39, 1532–1541,
1050   https://doi.org/10.1021/es048375y, 2005b.

Lim, Y. B., Tan, Y., Perri, M. J., Seitzinger, S. P., and Turpin, B. J.: Aqueous chemistry and its role in secondary organic aerosol (SOA) formation, Atmos. Chem. Phys., 10, 10521–10539, https://doi.org/10.5194/acp-10-10521-2010, 2010.

Ling, Z., Xie, Q., Shao, M., Wang, Z., Wang, T., Guo, H., and Wang, X.: Formation and sink of glyoxal and methylglyoxal in a polluted subtropical environment: observation-based photochemical analysis and impact evaluation, Atmos. Chem. Phys., 20, 11451–11467, https://doi.org/10.5194/acp-20-11451-2020, 2020.

Liu, C., Chu, B., Liu, Y., Ma, Q., Ma, J., He, H., Li, J., and Hao, J.: Effect of mineral dust on secondary organic aerosol yield and aerosol size in α-pinene/NOx photo-oxidation, Atmospheric Environment, 77, 781–789, https://doi.org/10.1016/j.atmosenv.2013.05.064, 2013.

Loeffler, K. W., Koehler, C. A., Paul, N. M., & De Haan, D. O. (2006). Oligomer Formation in Evaporating Aqueous Glyoxal and Methyl Glyoxal Solutions. Environmental Science & Technology, 40(20), 6318–6323. https://doi.org/10.1021/es060810w

Mahowald, N., Albani, S., Kok, J. F., Engelstaeder, S., Scanza, R., Ward, D. S., and Flanner, M. G.: The size distribution of desert dust aerosols and its impact on the Earth system, Aeolian Research, 15, 53–71, https://doi.org/10.1016/j.aeolia.2013.09.002, 2014.

Ng, N. L., Canagaratna, M. R., Jimenez, J. L., Chhabra, P. S., Seinfeld, J. H., and Worsnop, D. R.: Changes in organic aerosol composition with aging inferred from aerosol mass spectra, Atmos. Chem. Phys., 11, 6465–6474, https://doi.org/10.5194/acp-11-6465-2011, 2011.

Nie, W., Ding, A., Wang, T., Kerminen, V.-M., George, C., Xue, L., Wang, W., Zhang, Q., Petäjä, T., Qi, X., Gao, X., Wang, X., Yang, X., Fu, C., and Kulmala, M.: Polluted dust promotes new particle formation and growth, Sci Rep, 4, 6634, https://doi.org/10.1038/srep06634, 2014.

Nieder, R., Benbi, D. K., and Reichl, F. X.: Soil-Borne Particles and Their Impact on Environment and Human Health, in: Soil Components and Human Health, Springer Netherlands, Dordrecht, 99–177, https://doi.org/10.1007/978-94-024-1222-2_3, 2018.

Nozière, B., Dziedzic, P., and Córdova, A.: Products and Kinetics of the Liquid-Phase Reaction of Glyoxal Catalyzed by Ammonium Ions (NH$_4$ +), J. Phys. Chem. A, 113, 231–237, https://doi.org/10.1021/jp8078293, 2009.

Ooki, A. and Uematsu, M.: Chemical interactions between mineral dust particles and acid gases during Asian dust events, J. Geophys. Res., 110, 2004JD004737, https://doi.org/10.1029/2004JD004737, 2005.

Ortiz-Montalvo, D. L., Häkkinen, S. A. K., Schwier, A. N., Lim, Y. B., McNeill, V. F., and Turpin, B. J.: Ammonium Addition (and Aerosol pH) Has a Dramatic Impact on the Volatility and Yield of Glyoxal Secondary Organic Aerosol, Environ. Sci. Technol., 48, 255–262, https://doi.org/10.1021/es4035667, 2014.

Ponczek, M., Hayeck, N., Emmelin, C., and George, C.: Heterogeneous photochemistry of dicarboxylic acids on mineral dust, Atmospheric Environment, 212, 262–271, https://doi.org/10.1016/j.atmosenv.2019.05.032, 2019.

Romanias, M. N., El Zein, A., and Bedjanian, Y.: Heterogeneous Interaction of H$_2$O$_2$ with TiO$_2$ Surface under Dark and UV Light Irradiation Conditions, J. Phys. Chem. A, 116, 8191–8200, https://doi.org/10.1021/jp305366v, 2012.

Romanías, Manolis N., Habib Ourrad, Frédéric Thévenet, and Véronique Riffault. 2016. "Investigating the Heterogeneous Interaction of VOCs with Natural Atmospheric Particles: Adsorption of Limonene and Toluene on Saharan Mineral Dusts." The Journal of Physical Chemistry A 120(8):1197–1212. doi: 10.1021/acs.jpca.5b10323.

Rossignol, S., Aregahegn, K. Z., Tinel, L., Fine, L., Nozière, B., and George, C.: Glyoxal Induced Atmospheric Photosensitized Chemistry Leading to Organic Aerosol Growth, Environ. Sci. Technol., 48, 3218–3227, https://doi.org/10.1021/es405581g, 2014.

Rubasinghege, G., Ogden, S., Baltrusaitis, J., and Grassian, V. H.: Heterogeneous Uptake and Adsorption of Gas-Phase Formic Acid on Oxide and Clay Particle Surfaces: The Roles of Surface

1101   Hydroxyl Groups and Adsorbed Water in Formic Acid Adsorption and the Impact of Formic Acid
1102   Adsorption on Water Uptake, J. Phys. Chem. A, 117, 11316–11327,
1103   https://doi.org/10.1021/jp408169w, 2013.

1104 Safi Shalamzari, M., Ryabtsova, O., Kahnt, A., Vermeylen, R., Hérent, M., Quetin-Leclercq, J., Van Der
1105   Veken, P., Maenhaut, W., and Claeys, M.: Mass spectrometric characterization of organosulfates
1106   related to secondary organic aerosol from isoprene, Rapid Comm Mass Spectrometry, 27, 784–
1107   794, https://doi.org/10.1002/rcm.6511, 2013.

1108 Schwier, A. N., Sareen, N., Mitroo, D., Shapiro, E. L., and McNeill, V. F.: Glyoxal-Methylglyoxal Cross-
1109   Reactions in Secondary Organic Aerosol Formation, Environ. Sci. Technol., 44, 6174–6182,
1110   https://doi.org/10.1021/es101225q, 2010.

1111 Seisel, S., Lian, Y., Keil, T., Trukhin, M. E., and Zellner, R.: Kinetics of the interaction of water vapour
1112   with mineral dust and soot surfaces at T = 298 K, Phys. Chem. Chem. Phys., 6, 1926–1932,
1113   https://doi.org/10.1039/B314568A, 2004.

1114 Shapiro, E. L., Szprengiel, J., Sareen, N., Jen, C. N., Giordano, M. R., and McNeill, V. F.: Light-absorbing
1115   secondary organic material formed by glyoxal in aqueous aerosol mimics, Atmos. Chem. Phys.,
1116   2009.

1117 Shen, X., Wu, H., Zhao, Y., Huang, D., Huang, L., and Chen, Z.: Heterogeneous reactions of glyoxal on
1118   mineral particles: A new avenue for oligomers and organosulfate formation, Atmospheric
1119   Environment, 131, 133–140, https://doi.org/10.1016/j.atmosenv.2016.01.048, 2016.

1120 Shrivastava, M., Cappa, C. D., Fan, J., Goldstein, A. H., Guenther, A. B., Jimenez, J. L., Kuang, C.,
1121   Laskin, A., Martin, S. T., Ng, N. L., Petaja, T., Pierce, J. R., Rasch, P. J., Roldin, P., Seinfeld, J.
1122   H., Shilling, J., Smith, J. N., Thornton, J. A., Volkamer, R., Wang, J., Worsnop, D. R., Zaveri, R.
1123   A., Zelenyuk, A., and Zhang, Q.: Recent advances in understanding secondary organic aerosol:
1124   Implications for global climate forcing, Reviews of Geophysics, 55, 509–559,
1125   https://doi.org/10.1002/2016RG000540, 2017.

1126 Song, Q. and Osada, K.: Direct measurement of aerosol acidity using pH testing paper and hygroscopic
1127   equilibrium under high relative humidity, Atmospheric Environment, 261, 118605,
1128   https://doi.org/10.1016/j.atmosenv.2021.118605, 2021.

1129 Steinke, I., Funk, R., Busse, J., Iturri, A., Kirchen, S., Leue, M., Möhler, O., Schwartz, T., Schnaiter, M.,
1130   Sierau, B., Toprak, E., Ullrich, R., Ulrich, A., Hoose, C., and Leisner, T.: Ice nucleation activity of
1131   agricultural soil dust aerosols from Mongolia, Argentina, and Germany, JGR Atmospheres, 121,
1132   https://doi.org/10.1002/2016JD025160, 2016.

1133 Sun, Y. L., Zhang, Q., Anastasio, C., and Sun, J.: Insights into secondary organic aerosol formed via
1134   aqueous-phase reactions of phenolic compounds based on high resolution mass spectrometry,
1135   Atmos. Chem. Phys., 10, 4809–4822, https://doi.org/10.5194/acp-10-4809-2010, 2010.

1136 Tang, M., Huang, X., Lu, K., Ge, M., Li, Y., Cheng, P., Zhu, T., Ding, A., Zhang, Y., Gligorovski, S.,
1137   Song, W., Ding, X., Bi, X., and Wang, X.: Heterogeneous reactions of mineral dust aerosol:
1138   implications for tropospheric oxidation capacity, Atmos. Chem. Phys., 17, 11727–11777,
1139   https://doi.org/10.5194/acp-17-11727-2017, 2017.

1140 Tegen, I. and Fung, I.: Contribution to the atmospheric mineral aerosol load from land surface
1141   modification, J. Geophys. Res., 100, 18707, https://doi.org/10.1029/95JD02051, 1995.

1142 Trainic, M., Abo Riziq, A., Lavi, A., Flores, J. M., and Rudich, Y.: The optical, physical and chemical
1143   properties of the products of glyoxal uptake on ammonium sulfate seed aerosols, Atmos. Chem.
1144   Phys., 11, 9697–9707, https://doi.org/10.5194/acp-11-9697-2011, 2011.

1145 Turpin, B. J. and Huntzicker, J. J.: Identification of secondary organic aerosol episodes and quantitation
1146   of primary and secondary organic aerosol concentrations during SCAQS, Atmospheric
1147   Environment, 29, 3527–3544, https://doi.org/10.1016/1352-2310(94)00276-Q, 1995.

1148 Usher, C. R., Michel, A. E., and Grassian, V. H.: Reactions on Mineral Dust, Chem. Rev., 103, 4883–
1149   4940, https://doi.org/10.1021/cr020657y, 2003.

Volkamer, R., Platt, U., and Wirtz, K.: Primary and Secondary Glyoxal Formation from Aromatics: Experimental Evidence for the Bicycloalkyl−Radical Pathway from Benzene, Toluene, and p - Xylene, J. Phys. Chem. A, 105, 7865–7874, https://doi.org/10.1021/jp010152w, 2001.

Volkamer, R., Spietz, P., Burrows, J., and Platt, U.: High-resolution absorption cross-section of glyoxal in the UV–vis and IR spectral ranges, Journal of Photochemistry and Photobiology A: Chemistry, 172, 35–46, https://doi.org/10.1016/j.jphotochem.2004.11.011, 2005.

Volkamer, R., San Martini, F., Molina, L. T., Salcedo, D., Jimenez, J. L., and Molina, M. J.: A missing sink for gas-phase glyoxal in Mexico City: Formation of secondary organic aerosol, Geophysical Research Letters, 34, 2007GL030752, https://doi.org/10.1029/2007GL030752, 2007.

Vrekoussis, M., Wittrock, F., Richter, A., Burrows, J. P., and Cho, C.: Temporal and spatial variability of glyoxal as observed from space, Atmos. Chem. Phys., 2009.

Wagner, C., Hanisch, F., Holmes, N., de Coninck, H., Schuster, G., and Crowley, J. N.: The interaction of N2O5 with mineral dust: aerosol flow tube and Knudsen reactor studies, Atmos. Chem. Phys., 2008.

Walker, H., Stone, D., Ingham, T., Hackenberg, S., Cryer, D., Punjabi, S., Read, K., Lee, J., Whalley, L., Spracklen, D. V., Carpenter, L. J., Arnold, S. R., and Heard, D. E.: Observations and modelling of glyoxal in the tropical Atlantic marine boundary layer, Atmos. Chem. Phys., 22, 5535–5557, https://doi.org/10.5194/acp-22-5535-2022, 2022.

Wang, G., Cheng, C., Meng, J., Huang, Y., Li, J., and Ren, Y.: Field observation on secondary organic aerosols during Asian dust storm periods: Formation mechanism of oxalic acid and related compounds on dust surface, Atmospheric Environment, 113, 169–176, https://doi.org/10.1016/j.atmosenv.2015.05.013, 2015.

Wang, J., Doussin, J. F., Perrier, S., Perraudin, E., Katrib, Y., Pangui, E., and Picquet-Varrault, B.: Design of a new multi-phase experimental simulation chamber for atmospheric photosmog, aerosol and cloud chemistry research, Atmos. Meas. Tech., 4, 2465–2494, https://doi.org/10.5194/amt-4-2465-2011, 2011.

Washenfelder, R. A., Young, C. J., Brown, S. S., Angevine, W. M., Atlas, E. L., Blake, D. R., Bon, D. M., Cubison, M. J., De Gouw, J. A., Dusanter, S., Flynn, J., Gilman, J. B., Graus, M., Griffith, S., Grossberg, N., Hayes, P. L., Jimenez, J. L., Kuster, W. C., Lefer, B. L., Pollack, I. B., Ryerson, T. B., Stark, H., Stevens, P. S., and Trainer, M. K.: The glyoxal budget and its contribution to organic aerosol for Los Angeles, California, during CalNex 2010: GLYOXAL BUDGET FOR LOS ANGELES, J. Geophys. Res., 116, https://doi.org/10.1029/2011JD016314, 2011.

Webb, N. P. and Pierre, C.: Quantifying Anthropogenic Dust Emissions, Earth's Future, 6, 286–295, https://doi.org/10.1002/2017EF000766, 2018.

Xu, K., Liu, Y., Li, C., Zhang, C., Liu, X., Li, Q., Xiong, M., Zhang, Y., Yin, S., and Ding, Y.: Enhanced secondary organic aerosol formation during dust episodes by photochemical reactions in the winter in Wuhan, Journal of Environmental Sciences, 133, 70–82, https://doi.org/10.1016/j.jes.2022.04.018, 2023.

Zeineddine, M. N., Romanias, M. N., Gaudion, V., Riffault, V., and Thévenet, F.: Heterogeneous Interaction of Isoprene with Natural Gobi Dust, ACS Earth Space Chem., 1, 236–243, https://doi.org/10.1021/acsearthspacechem.7b00050, 2017.

Zeineddine, M. N., Urupina, D., Romanias, M. N., Riffault, V., and Thevenet, F.: Uptake and reactivity of acetic acid on Gobi dust and mineral surrogates: A source of oxygenated volatile organic compounds in the atmosphere?, Atmospheric Environment, 294, 119509, https://doi.org/10.1016/j.atmosenv.2022.119509, 2023.

Zhang, X., He, A., Guo, R., Zhao, Y., Yang, L., Morita, S., Xu, Y., Noda, I., and Ozaki, Y.: A new approach to removing interference of moisture from FTIR spectrum, Spectrochimica Acta Part A: Molecular and Biomolecular Spectroscopy, 265, 120373, https://doi.org/10.1016/j.saa.2021.120373, 2022.

Zhang, Y., He, L., Sun, X., Ventura, O. N., & Herrmann, H. (2022). Theoretical Investigation on the Oligomerization of Methylglyoxal and Glyoxal in Aqueous Atmospheric Aerosol Particles. ACS

1200 Earth and Space Chemistry, 6(4), 1031–1043.
1201 https://doi.org/10.1021/acsearthspacechem.1c00422

1202 Zielinski, A. T., Kourtchev, I., Bortolini, C., Fuller, S. J., Giorio, C., Popoola, O. A. M., Bogialli, S.,
1203 Tapparo, A., Jones, R. L., and Kalberer, M.: A new processing scheme for ultra-high resolution
1204 direct infusion mass spectrometry data, Atmospheric Environment, 178, 129–139,
1205 https://doi.org/10.1016/j.atmosenv.2018.01.034, 2018.

1206

1207